AIAA 2003-3169

Development of a Jet Noise Prediction Method for Installed Jet Configurations

Craig A. Hunter and Russell H. Thomas
NASA Langley Research Center
Hampton, Virginia

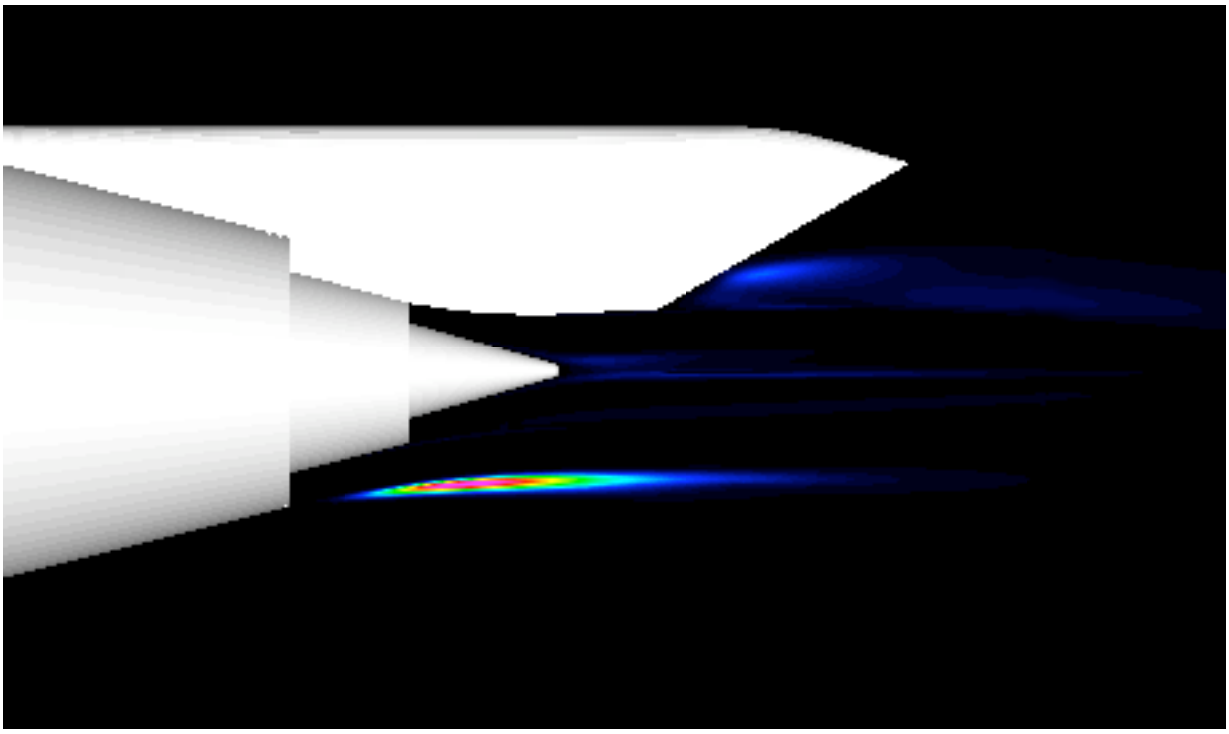

9th AIAA/CEAS Aeroacoustics Conference and Exhibit
12-14 May 2003 / Hilton Head, SC

Development of a Jet Noise Prediction Method for Installed Jet Configurations

Craig A. Hunter† and Russell H. Thomas‡
NASA Langley Research Center - Hampton, Virginia USA

Abstract

This paper describes development of the Jet3D noise prediction method and its application to heated jets with complex three-dimensional flow fields and installation effects. Noise predictions were made for four separate flow bypass ratio five nozzle configurations tested in the NASA Langley Jet Noise Laboratory. These configurations consist of a round core and fan nozzle with and without pylon, and an eight chevron core nozzle and round fan nozzle with and without pylon. Predicted SPL data were in good agreement with experimental noise measurements up to 121° inlet angle, beyond which Jet3D under predicted low frequency levels. This is due to inherent limitations in the formulation of Lighthill's Acoustic Analogy used in Jet3D, and will be corrected in ongoing development. Jet3D did an excellent job predicting full scale EPNL for non-chevron configurations, and captured the effect of the pylon, correctly predicting a reduction in EPNL. EPNL predictions for chevron configurations were not in good agreement with measured data, likely due to the lower mixing and longer potential cores in the CFD simulations of these cases.

Introduction

In recent decades, there have been significant advances in aircraft noise reduction efforts. Many noise reduction strategies and devices have been developed and implemented, bringing current aircraft to noise levels about 20dB below those of first generation aircraft. Much of the acoustics research in the past has been concentrated at the component level in understanding the physics of noise generation, formulating noise prediction methods, and developing noise reduction strategies based on these advances. In general, additional decibels of noise reduction are increasingly costly to obtain as so many of the ideas from the last several decades have been investigated. This reality has forced new strategies. One new strategy in NASA's noise reduction program is a focus on the noise effects specifically attributable to installation. This focus will also extend to developing noise reduction strategies that take advantage of installation effects.

For jet exhaust noise, installation effects can include those due to the pylon-jet interaction, wing downwash, and flap-jet interaction. Therefore, an essential requirement for an installed jet noise prediction method is that it must be able to predict noise from complex three-dimensional flows. Having this physics based capability is also desirable in order to develop a flexible noise prediction method applicable to the investigation of advanced concepts and revolutionary configurations.

A jet noise prediction tool satisfying these objectives is currently under development at NASA Langley Research Center. The "Jet3D" methodology is based on Lighthill's Acoustic Analogy and uses Reynolds-averaged Navier-Stokes (RANS) computational fluid dynamics (CFD) simulations from the PAB3D flow solver, with temperature-corrected two-equation k-ε turbulence closure and anisotropic Reynolds stress modeling. Jet3D has been formulated as a general three-dimensional method and has no restrictions on the type of flow field or nozzle geometry used for noise prediction. Furthermore, the Reynolds stress models used in PAB3D and Jet3D calculate six independent Reynolds stresses in an effort to properly address the anisotropic nature of 3D jet flows. This is particularly essential to capture the noise generated by complex geometries and installation effects.

In addition to its noise prediction capabilities, Jet3D has been developed as an aeroacoustic design and analysis tool, allowing the user to perform advanced flow field diagnostics and noise source identification. With visualization software, a researcher can use Jet3D to interrogate the flow and noise fields, creating a powerful tool that couples aerodynamics and aeroacoustics. This tool has been developed for use in the configuration aerodynamics and propulsion airframe integration disciplines.

The theoretical formulation, background, and basic validation of Jet3D have been reported in detail by Hunter in a previous publication [1], and will only be summarized briefly here. The main focus of this paper is the application of Jet3D to heated jets with complex three-dimensional flow fields and installation effects. Results will be discussed from noise predictions made for four separate flow bypass ratio five nozzle configurations tested in the NASA Langley Jet Noise Laboratory. These cases represent a significant progression in the development of Jet3D's noise prediction capability.

† Aerospace Engineer - Configuration Aerodynamics Branch. ‡ Aerospace Engineer - Aeroacoustics Branch, Senior Member AIAA.

Nomenclature

α_c	Jet convection factor parameter
α_L	Length scale calibration constant
α_τ	Time scale calibration constant
c	Local speed of sound (m/s)
c_∞	Ambient speed of sound (m/s)
C	Local jet convection factor
C_∞	Flight convection factor
D	Core nozzle diameter (m)
δ_{ij}	Kronecker delta function
ε	Dissipation rate of k (m^2/s^3)
g	Temporal correlation function, $g = g(\eta)$
k	TKE per unit mass (m^2/s^2)
ℓ_1, ℓ_2, ℓ_3	Turbulence length scales (m)
$\vec{M}_c$	Jet convection Mach number vector
$\vec{M}$	Flight Mach number vector
M_e	Jet Exit Mach number
M_1	Local Axial Mach number
β	Correlation calibration constant
NPR	Nozzle Pressure Ratio
p	Fluctuating acoustic pressure (N/m^2)
P	Static pressure (N/m^2)
P_o	Stagnation pressure (N/m^2)
θ	Observer angle from jet axis (deg)
θ^*	Snell's Law critical angle (deg)
$\vec{r}$	Acoustic radius vector (m), $\vec{r} = \vec{x} - \vec{z}$
r	Magnitude of $\vec{r}$ (m)
$\hat{r}$	Acoustic radius unit vector, $\hat{r} = \vec{r}/r$
R_{im}	Spatial correlation function
ρ	Density (kg/m^3)
σ_{ij}	Viscous stress tensor (N/m^2)
t	Time (s)
T	Temperature (°K)
T_{ij}	Lighthill stress tensor (N/m^2)
T_o	Stagnation temperature (°K)
T_∞	Freestream static temperature (°K)
TKE	Turbulent Kinetic Energy
τ	Time delay in observer frame (s)
η	Moving frame time delay (s), $\eta = \tau - \xi/C$
τ_o	Characteristic time scale of turbulence (s)
$\vec{u}$	Total velocity (m/s), $\vec{u}(\vec{z},t) = \vec{V}(\vec{z}) + \vec{v}(\vec{z},t)$
$\vec{v}$	Turbulent velocity (m/s), $\vec{v} = \vec{v}(\vec{z},t)$
$\vec{V}$	Mean flow velocity (m/s), $\vec{V} = \vec{V}(\vec{z})$
V_∞	Freestream velocity (m/s)
$\langle v_i v_m \rangle$	One-point turb. velocity correlation (m^2/s^2)
$\langle v_i v_m' \rangle$	Two-point turb. velocity correlation (m^2/s^2)
$\vec{x}$	Fixed observer position vector (m)
X	Jet Axis for Noise Source Plots (m)
Y	Vertical Axis for Noise Source Plots (m)
$\vec{z}$	Moving frame source position vector (m)
Z	Spanwise Axis for Noise Source Plots (m)
$\vec{\xi}$	Moving frame separation vector (m)

Notes:

1. η, $\vec{z}$, and $\vec{\xi}$ are in a reference frame locally convecting downstream at $\vec{M}_c$.
2. For a generic quantity q, $\langle q \rangle$ represents a time average and qq' represents a two-point space-time correlation between $q(\vec{z},t)$ and $q'(\vec{z}+\vec{\xi}, t+\tau)$.

Background

Jet3D is based on a straightforward application of Lighthill's Acoustic Analogy in three dimensions, shown here solved and manipulated to give the far field mean-square acoustic pressure:

$$\langle p^2 \rangle(\vec{x},\tau) = \frac{1}{16\pi^2 c^4} \int_{JET} \int \frac{\hat{r}_i \hat{r}_j \hat{r}_m \hat{r}_n}{C\ C^5 r^2} \int \frac{\partial^4}{\partial \tau^4} \langle T_{ij} T'_{mn} \rangle d\eta\, d\vec{z}$$

where $T_{ij} = (p - c^2\rho)\delta_{ij} - \sigma_{ij} + \rho u_i u_j$ is the Lighthill Stress Tensor. Developed over fifty years ago [2,3], this elegant theory unified the fields of aerodynamics and acoustics. In deriving the acoustic analogy, Lighthill cast the complicated nonlinear jet noise problem into a simple analogy with classical acoustics; the flow field and complex flow-acoustic interactions (such as sound wave convection and refraction) in a real jet are replaced by a fictitious volume source distribution of acoustic quadrupoles radiating into a uniform ambient medium.

Though powerfully simple in its approach, Lighthill's Acoustic Analogy has been difficult to implement for complex jet flows over the past fifty years. The chief difficulty is due to the tacit assumption that the mean flow and fluctuating turbulent fields in a jet – namely, components of the Lighthill Stress Tensor T_{ij} – are known. Full knowledge of the jet flow field remains elusive to this day, but advances in computational fluid dynamics have closed the gap quite a bit. In addition, the quality of information available in a jet RANS-CFD simulation has improved to the point where it is now possible to develop better models and make educated assumptions about the remaining unknowns.

By following Lighthill's assumption that the stress tensor can be approximated as $T_{ij} \sim \rho u_i u_j$, breaking velocities out into mean and fluctuating components $u_i(\vec{z},t) = V_i(\vec{z}) + v_i(\vec{z},t)$, and assuming that density is only a function of space, i.e., $\rho(\vec{z},t) \approx \rho(\vec{z})$, the two-point time-delayed correlation of the Lighthill Stress tensor becomes:

$$\frac{\partial^4}{\partial \tau^4} \langle T_{ij} T'_{mn} \rangle = \rho^2 \frac{\partial^4}{\partial \tau^4} \left[4 V_j V'_n \langle v_i v'_m \rangle + \langle v_i v_j v'_m v'_n \rangle \right]$$

Note that odd terms involving triple correlations of the form $\langle v_i v_j v_k \rangle$ have been dropped, on the assumption that they would integrate to zero under the correlation integral. Of the two remaining terms, the first is known as the "shear noise" term, since it arises from interactions between turbulent and mean flow velocities. The second term is the "self noise" terms, as it arises from interactions between the turbulent velocities themselves. Under the assumption that the joint probability distribution of turbulent velocities is normal, the quadruple self noise correlation can be expanded into the product of double correlations as shown by Batchelor [4]:

$$\langle v_i v_j v_m v_n \rangle = \langle v_i v_j \rangle \langle v_m v_n \rangle + \langle v_i v_m \rangle \langle v_j v_n \rangle + \langle v_i v_n \rangle \langle v_j v_m \rangle$$

From this point onward, implementation of the Lighthill theory in Jet3D centers on the modeling of two-point space-time correlations for shear and self noise terms. Mean flow correlations for velocity and density are modeled using a Taylor series expansion, written in terms of local mean flow gradients and the separation vector of correlation:

$$\rho \sim \rho + \ell_k \frac{\partial \rho}{\partial z_k} \qquad V_n \sim V_n + \ell_k \frac{\partial V_n}{\partial z_k}$$

Turbulent velocity correlations are separated into space and time factors and modeled using the local one-point correlation (related to the Reynolds stress tensor) and a combination of Gaussian-type exponential functions and quadratic functions:

$$\langle v_i v_n \rangle = \langle v_i v_m \rangle R(\vec{z}, \vec{\ell}) \, g(\vec{z}, \tau)$$

where

$$R(\vec{z}, \vec{\ell}) = \frac{1}{\pi^2} \frac{\ell_1^2}{\ell_1^2} + \frac{\ell_2^2}{\ell_2^2} + \frac{\ell_3^2}{\ell_3^2} \exp\left[-\left(\frac{\ell_1^2}{\ell_1^2} + \frac{\ell_2^2}{\ell_2^2} + \frac{\ell_3^2}{\ell_3^2} \right) \right]$$

$$g(\vec{z}, \tau) = \exp\left\{ -\tau^2 / \tau_o^2 \right\}$$

Here, τ_o is a characteristic time scale of turbulence:

$$\tau_o = \alpha_\tau \frac{k}{\varepsilon}$$

and ℓ_1, ℓ_2, and ℓ_3 are characteristic length scales of turbulence:

$$\ell_1 = \alpha_L \frac{\langle v_1^2 \rangle^{3/2}}{\varepsilon} \qquad \ell_2 = \alpha_L \frac{\langle v_2^2 \rangle^{3/2}}{\varepsilon} \qquad \ell_3 = \alpha_L \frac{\langle v_3^2 \rangle^{3/2}}{\varepsilon}$$

In the present study, where a linear Reynolds stress model is used to obtain $\langle v_i v_m \rangle$, the following fixed values were used for the three calibration constants:

$$C = 0.735 \qquad \alpha_\tau = 0.15 \qquad \alpha_L = 0.34$$

Both C and α_τ are consistent with values used during early validation of Jet3D for the noise prediction of supersonic round jets [1]. In that earlier work, a slightly different $\alpha_L = 0.3$ was used with a nonlinear Reynolds stress model.

After carrying out tensor products with $\hat{r}_i \hat{r}_j \hat{r}_m \hat{r}_n$, and putting everything together, the mean-square acoustic pressure can be written as:

$$\langle p^2 \rangle(\vec{x}, \tau) = \langle p^2 \rangle_{\text{SHEAR}}(\vec{x}, \tau) + \langle p^2 \rangle_{\text{SELF}}(\vec{x}, \tau)$$

where

$$\langle p^2 \rangle_{\text{SHEAR}}(\vec{x}, \tau) = \frac{1}{16\pi^2 c^4} \int_{\text{JET}} \frac{4\pi V_r \langle v_r v_r \rangle}{C \, C^5 r^2} G_{\text{SHEAR}}(\vec{z}, \tau) \int_\tau F_{\text{SHEAR}}(\vec{z}, \vec{\ell}) \, d\vec{\ell} \, d\vec{z}$$

$$\langle p^2 \rangle_{\text{SELF}}(\vec{x}, \tau) = \frac{1}{16\pi^2 c^4} \int_{\text{JET}} \frac{2\pi \langle v_r v_r \rangle^2}{C \, C^5 r^2} G_{\text{SELF}}(\vec{z}, \tau) \int_\tau F_{\text{SELF}}(\vec{z}, \vec{\ell}) \, d\vec{\ell} \, d\vec{z}$$

$$\hat{r}_i \hat{r}_m \langle v_i v_m \rangle = \langle v_r v_r \rangle \qquad \hat{r}_j V_j = V_r$$

and the various functions are defined in [1]. The remaining analysis is straightforward but tedious, so the reader is referred to [1] for details. In summary, the following steps are carried out:

1. $\vec{\ell}$ correlation integrals are evaluated.

2. A Fourier transform is applied to obtain the spectral density of the mean-square acoustic pressure.

3. The spectral density is integrated over a frequency band to obtain the mean-square acoustic pressure spectrum in that band.

The remaining $\vec{z}$ integration over the jet is evaluated numerically. Thus, the Jet3D noise prediction algorithm is based on the volume integration over a jet of equations giving the band-integrated mean-square acoustic pressure spectrum for the shear and self noise. The integration is carried out for each volume element in a discretized jet flow field using data obtained from a CFD solution. Within the integration routine, turbulent Reynolds stresses are

computed using one of several linear or nonlinear anisotropic models [1], atmospheric absorption effects are calculated with the Shields and Bass attenuation model [5], mean flow gradients are computed with a finite volume scheme [1], and local convection Mach number (M_c) is modeled empirically using correlated data trends from the classic Davies experiment [1,6]:

$$\frac{M_c - M}{M_e - M} = 0.13 + 1.18\left(\frac{M_1 - M}{M_e - M}\right) - 0.62\left(\frac{M_1 - M}{M_e - M}\right)^2$$

In the present formulation of Jet3D, the Ribner/Ffowcs-Williams [7,8] jet convection factor is used:

$$C = \left[(1 - M_c \cos\theta)^2 + \beta_c^2 M_c^2\right]^{1/2}$$
$$(\beta_c = 0.58)$$

along with the $C = |1 + M\cos\theta|$ forward flight convection factor.

A recent modification to Jet3D corrects for flow–acoustic interaction effects (i.e., sound wave convection and refraction) not properly modeled in the current Jet3D implementation of Lighthill's Acoustic Analogy. It is important to note that these effects are present in the exact version of Lighthill's Acoustic Analogy, and work is underway to reformulate Jet3D to properly reflect this. Based on experience gained through development and testing, it has become clear that spatial phasing of quadrupole sources in the jet flow will reconstruct flow–acoustic interaction effects in the jet arc, including the well observed zone of silence. This will be discussed in more detail in a future paper.

In the meantime, a rather simple modification based on elementary ray tracing improves predictions in the jet arc. Using Snell's Law [9], the critical angle defining a zone of silence for wave propagation between a source within the jet flow and the outside ambient medium is given by:

$$\theta^* = \cos^{-1}\left[\frac{c}{c + V}\right]$$

This critical angle is computed for every cell within the jet flow, using local conditions for velocity (V) and speed of sound (c). For the cases discussed in this paper, the critical angle ranged from approximately $\theta^*=30°$ to $\theta^*=60°$ (150° to 120° inlet angle) in noisemaking regions of the jet. At angles outside the zone of silence ($\theta > \theta^*$), the standard Jet3D theory is applied. Within the zone of silence ($\theta < \theta^*$), noise sources are simply ignored. Though this is a rather crude approximation, it appears to work reasonably well in a number of test cases. This approximation is most valid at high frequencies, where the wavelength of radiated noise is small compared to the jet's width and flow-acoustic interaction effects do in fact "filter" high frequency noise from observers in the zone of silence. Conversely, the approximation is most questionable at low frequencies where sound waves generally travel through a jet unaffected by the flow.

Jet3D is written in a combination of FORTRAN 77/90/95 and ANSI C with dynamic memory allocation, and is easily ported across numerous Unix/Linux platforms. Recent development work has led to a vectorized multiprocessor version of Jet3D optimized for PowerMac G4 computers running the Unix-based Mac OS X [10] operating system. As a result of the multi-gigaflop vector performance on this platform, noise predictions for the complex configurations discussed in this paper (on the order of 32 million cells for the full 3D jet) took less than 2 minutes per observer on a 1.25Ghz dual processor PowerMac G4 workstation. Output data was written in text and binary files, suitable for post processing and visualization.

Experiment and Nozzle Configurations

In this paper, Jet3D noise predictions are compared to experimental acoustic data obtained in the Low Speed Aeroacoustics Wind Tunnel (LSAWT) at NASA Langley's Jet Noise Laboratory (JNL). Figure 1 shows the baseline nozzle (Configuration 1) installed on the jet engine simulator (JES) in the wind tunnel. The JES is a dual stream propulsion system with two independently controlled air streams, each equipped with propane burners. The wind tunnel has a 1.43m square test section that simulates forward flight over the JES, and is lined with acoustic wedges producing a cut-off frequency of 125 Hz.

Experimental data are presented for four separate flow bypass ratio (BPR) five nozzle configurations operating at the takeoff cycle point with a freestream Mach number of 0.28. Each 1/9-scale nozzle has a nominal core exit diameter of D=0.128m. These configurations are shown in detail in figures 2–5, and consist of a baseline round core and fan nozzle (Configuration 1), a round core and fan nozzle with a pylon and lower fan bifurcator strut (Configuration 6), an eight chevron core nozzle with a round fan nozzle (Configuration 3), and an eight chevron core nozzle with a round fan nozzle, pylon, and lower fan

bifurcator strut (Configuration 4F). The nozzle, pylon, and chevron designs are not from a specific engine, but rather, they are typical of BPR 5 engines. The chevrons are designed to penetrate into the core flow by approximately the thickness of the boundary layer. In configuration 4F, the tip of a chevron is aligned with the pylon symmetry plane. Additional details of the configurations can be found in [11,12].

At the takeoff test point, the following nominal conditions were used:

$$\textit{Core Nozzle: } NPR=1.56,\ T_o=828°K$$

$$\textit{Fan Nozzle: } NPR=1.75,\ T_o=359°K$$

$$\textit{Freestream: } P_o=101353 N/m^2,\ T_o=295°K,\ M_\infty=0.28$$

Note that data presented for all the configurations were obtained at the same cycle point. As a result, thrust of pylon configurations is less than the thrust of non-pylon configurations by an amount related to the area that the pylon subtracts from the fan nozzle stream. Relative to the baseline nozzle, this pylon effect reduces fan thrust by about 6.8% and total thrust by about 6%.

Acoustic data were collected with a 28 microphone sideline array located 3.52m from the centerline axis of the model. Data presented in this report were obtained with nozzle pylons positioned 90° relative to the sideline array. Microphones were 6.35mm in diameter, operated with the grid caps removed, and calibrated with a piston phone and electrostatic calibrator before and after the test. Acoustic data shown in subsequent sections are processed to 1/3 octave bands and include corrections for the microphone calibration, wind tunnel background noise, shear layer refraction, a Doppler shift to the spectral data, and atmospheric absorption to acoustic standard day conditions of T=298°K, P=101357N/m^2, and 70% relative humidity.

JNL SPL data are presented at model scale, propagated to a 100D circular arc centered on the core nozzle exit, and have a standard deviation of ±0.47dB. For a meaningful evaluation of results and comparison between configurations, full scale (scale factor 9.0) EPNL data were also computed for a M=0.28 flyover at a distance of 543m (1782ft), typical of certification. This corresponds to an altitude of 305m (1000ft) and a ground sideline distance of 450m (1476ft). EPNL data have a standard deviation of ±0.36 EPNdB.

Jet Noise Prediction

For SPL comparisons, Jet3D noise predictions were made at 24 observer locations along a 100D radius arc, at inlet angles ranging from 52° to 148°. At each observer point, 1/3 octave band frequency spectrum SPL were computed over center frequencies ranging from 200Hz to 100kHz. Though not presented in detail here, additional sideline predictions were made at full scale (scale factor 9.0), and fed through JNL data processing routines to come up with EPNL predictions for all four configurations. All Jet3D noise predictions were calculated following procedures, corrections, and conditions consistent with the JNL experimental data.

Computational Fluid Dynamics Simulation

The RANS-CFD simulations of Massey, et al. [12] were used as input data for noise prediction with Jet3D. These simulations were run with the PAB3D multi–block structured flow solver [13], using temperature-corrected two-equation k-ε turbulence closure [12,14] and a linear Reynolds stress model. Grid sizes ranged from 5.8 million cells for the half-span grid of Configuration 1 up to 16.2 million cells for the half-span grid of Configuration 4F. In all cases, the computational domain extended roughly 32D downstream of the fan nozzle exit and 6D from the centerline in the radial direction.

As discussed by Massey, et al. [12], CFD results were in excellent agreement with experimental mean flow total temperature and total pressure data for Configuration 1, and showed reasonably good agreement in the chevron configurations 3 and 4F, with lower mixing levels than seen in the experiment. Based on the jet potential core lengths, the Configuration 3 simulation was under-mixed by less than 1D, while Configuration 4F was under-mixed by 1-2D. Experimental flowfield data was not obtained for Configuration 6, but it is expected that this non-chevron case would also show excellent agreement between experiment and CFD.

It should be noted that experimental turbulence data has not been obtained for any of these configurations yet. Thus, full validation of the CFD solutions (from a turbulence and noise prediction standpoint) has not been conducted. This will be addressed with future PIV testing in the Langley Jet Noise Lab.

Grid Dependence Study

Prior to detailed noise prediction work, a study was conducted to evaluate possible grid dependence effects on the jet noise prediction for Configuration 1. As part of the normal mesh sequencing procedure used in PAB3D, solutions are advanced through coarse (1/4 resolution), medium (1/2 resolution), and fine (full resolution) grids. For validation purposes, an additional "extra fine" grid was generated with twice the resolution of the fine grid. SPL results from noise prediction for each of these grid levels are shown in figure 6, computed on the 100D arc at an inlet angle of 88°. There are notable differences between the coarse and medium grid levels and medium and fine grid levels (especially at high frequencies), but little to no difference between the fine and extra fine grid levels. Thus, the fine grid level appears suitable for noise prediction computations.

Results and Discussion

Jet3D predicted model-scale SPL results for Configurations 1, 6, 3, and 4F are given in figures 7A-7L, 8A-8L, 9A-9L, and 10A-10L, respectively. Predictions are compared to JNL model-scale data at observer inlet angles of 52°, 62°, 69°, 78°, and 88° in the inlet arc, and inlet angles of 98°, 109°, 121°, 127°, 134°, 141°, and 148° in the jet arc. For all 4 configurations, Jet3D predictions are in good to excellent agreement with JNL data in the inlet arc, but the agreement progressively deteriorates in the jet arc past about 121°, where Jet3D consistently under predicts low frequency SPL levels. This is undoubtedly due to the crude Snell's Law correction scheme used for flow-acoustic interaction effects in the jet arc, which is most valid at high frequencies and least valid at low frequencies. Note, however, that Jet3D would have over predicted most of the entire spectrum were it not for this correction. Jet arc predictions should improve when the correction is replaced with a revised Lighthill formulation where flow-acoustic interaction effects are properly captured through spatial source phasing.

Amongst the various configurations, Configurations 1 and 6 were seen to have slightly better SPL predictions than Configurations 3 and 4F, though this type of evaluation is highly dependent on frequency and observer angle. As discussed previously, the CFD simulations of Configuration 3 and 4F exhibited lower mixing than seen in experimental data, and this disparity seems to have translated directly into the noise prediction at certain angles and frequencies.

Full scale EPNL data are compared in Figure 11. Comparisons for non-chevron configurations 1 and 6 are very good; in both cases, Jet3D predictions are within the ±0.36 EPNdB standard deviation of JNL measurements. Furthermore, Jet3D properly captures the effect of the pylon (due in part to the reduced thrust of that configuration), predicting 0.69 EPNdB noise reduction. Note that the scale factor (which shifts model scale frequencies down by a factor of 9.0) and the EPNL calculation (which weights the frequencies in the audibly sensitive range) combine to de-emphasize the low frequency mis-match seen in model scale SPL data, resulting in the excellent comparison of EPNL between JNL measurements and Jet3D predictions for configurations 1 and 6.

Results for chevron configurations 3 and 4F are not as good; here, Jet3D misses both the absolute predictions and the relative differences. Configuration 3 is over predicted by 1.17 EPNdB, and Configuration 4F is under predicted by 0.63 EPNdB. What's more, a 0.54 EPNdB increase in noise was measured going from configurations 3 to 4F, while Jet3D predicted a 1.26 EPNdB decrease. These discrepancies are likely due to lower mixing levels and longer potential cores (compared to experiment) seen in the CFD simulations of these two cases. For example, going from Configuration 1 to Configuration 3, measurements show a 1.32 EPNdB reduction attributed to chevrons while Jet3D predicted only a 0.32 EPNdB reduction, so clearly the full effect of the chevrons is not being captured. Additional pylon/chevron flowfield interactions (see [11,12] for more details) are likely responsible for the other differences seen in Configuration 4F.

As an example of Jet3D's diagnostics capabilities, 8000Hz noise source maps are shown for each of the four configurations. X-Y symmetry plane maps are given in figures 12-15, and Y-Z crossflow plane maps are given in figures 16-19 at X/D locations of 1, 2, 3, and 4 (for reference, the fan nozzle exit is at X/D=0 and the core nozzle exit is at X/D~0.9). In these plots, color contours of mean-square acoustic pressure per unit volume emitted from the jet in the 8000Hz 1/3 octave band are shown at an observer angle of 121° on a 100D radius (observer located in the X-Z plane as noted in figure captions). Jet3D SPL predictions were reasonably good for all four configurations at this angle, with little to no negative impact from flow-acoustic interactions (thus, the Snell's Law correction does not affect these results). The 8000Hz band was chosen simply because it was amenable to discussion; similar analysis could be conducted at other frequencies.

Essentially, these figures show the noise emitted from the jet, traced back to the source and plotted per unit volume (to remove grid dependence). It is important to note that these sources are a direct result of Lighthill's Acoustic Analogy and its fictitious quadrupole distribution, and are not physical noise sources. However, there is still a direct relationship between the jet flow, the quadrupole sources, and far field noise, so these noise maps can be physically interpreted to a certain extent.

Looking at figures 12-15, noise in the 8000Hz band is seen to primarily originate from the fan flow shear layer from 0.5D to about 4D downstream of the fan nozzle exit. It is interesting to note that the noise source levels of configuration 4F are visibly lower than the other cases, confirming previously discussed results. Additional weak noise sources are seen near the plug in all configurations (due to plug separation) and around the pylon in configurations 6 and 4F. As discussed in [11], a high TKE spot formed downstream of the pylon where the split fan shear layers merge and the core shear layer is pulled upward by the pylon wake. In addition, interactions between the pylon and the fan flow give rise to vortices rolling off the pylon shelf corners [12]. Though these may not be considered traditional sources of jet noise, they impact the jet's mixing and shear flow characteristics and lead to jet noise. This is a prime example of an installation effect.

Examination of the crossflow noise maps in figures 16-19 reveals many interesting features. Of course, some of these are due to inherent asymmetries in the configurations and their jet flows (the reader is referred to [11,12] for more details about the jet flow fields). However, the noise maps show a strong pattern of acoustic asymmetry that goes beyond flow and nozzle asymmetry. These are evident in cases where the jet flow is axisymmetric (Configuration 1), periodically-axisymmetric (Configuration 3), and spanwise-symmetric (Configurations 6 and 4F). These patterns are a direct result of the spatial phasing in Lighthill's Acoustic Analogy, which comes about through dot products and tensor sums in the various shear and self noise terms. Thus, even an axisymmetric jet flow like the one of Configuration 1 has an asymmetric noise source distribution. It is this spatial phasing and resulting asymmetry that allows Lighthill's Acoustic Analogy to reconstruct complicated jet noise signatures from a simple volume source distribution of acoustic quadrupoles.

Conclusion

This paper describes development of the Jet3D noise prediction method and its application to heated jets with complex three-dimensional flow fields and installation effects. Noise predictions were made for four separate flow bypass ratio five nozzle configurations tested in the NASA Langley Jet Noise Laboratory. Jet3D SPL results were in good agreement with experimental noise measurements in the inlet arc. Jet arc predictions were decent up to about 121° inlet angle, beyond which Jet3D under predicted low frequency SPL levels. This is due to inherent limitations in the implementation of Lighthill's Acoustic Analogy used in Jet3D and the very crude approximation made to correct these limitations. Ongoing development of Jet3D will address these issues.

Based on full scale comparisons with measured data, Jet3D did a very good job predicting EPNL for non-chevron configurations 1 and 6, to within the standard deviation band of measured data. Furthermore, Jet3D captured the effect of the pylon, correctly predicting a reduction in EPNL. Jet3D EPNL predictions for chevron configurations 3 and 4F were not in as good agreement with measured data, likely due to the lower mixing and longer potential cores in the CFD simulations of these two cases.

Examination of noise source maps reveals many interesting features, and illustrates Jet3D's growing capability as an advanced diagnostic tool. The noise maps show a strong pattern of acoustic asymmetry that goes beyond flow and nozzle asymmetry. These patterns are a direct result of the spatial phasing in Lighthill's Acoustic Analogy, which allows Jet3D to effectively reconstruct complicated jet noise signatures from a simple volume source distribution of acoustic quadrupoles radiating into a uniform ambient medium. Jet noise prediction methods based on Lighthill's Acoustic Analogy must properly reproduce this effect to achieve valid results.

Acknowledgements

The authors would like to thank Steve Massey and Alaa Elmiligui of Eagle Aeronautics, and S. Paul Pao and K.S. Abdol-Hamid of NASA Langley Research Center for their many inputs to this work. The contributions by the entire Jet Noise Lab Team to the Pylon Effects Experiment are gratefully acknowledged.

References

1. Hunter, C.A. "An Approximate Jet Noise Prediction Method based on Reynolds-Averaged Navier-Stokes Computational Fluid Dynamics Simulation". D.Sc. Dissertation, The George Washington University, January 2002.

2. Lighthill, M.J. "On Sound Generated Aerodynamically: I. General Theory". *Proceedings of the Royal Society of London*, Series A, Volume 211, 1952, pp. 564-587.

3. Lighthill, M.J. "On Sound Generated Aerodynamically: II. Turbulence as a Source of Sound". *Proceedings of the Royal Society of London*, Series A, Volume 222, 1954, pp.1-32.

4. Batchelor, G.K. *The Theory of Homogeneous Turbulence*. Cambridge, England: Cambridge University Press, 1953.

5. Shields, F.D., and Bass, H.E. "Atmospheric Absorption of High Frequency Noise and Application to Fractional Octave Bands". NASA CR-2760, June 1977.

6. Davies, P.O.A.L., Fisher, M.J., and Barrat, M.J. "The Characteristics of the Turbulence in the Mixing Region of a Round Jet". *Journal of Fluid Mechanics*, Vol. 15, March 1963, pp. 337–367.

7. Ribner, H.S. "The Generation of Sound by Turbulent Jets". *Advances in Applied Mechanics*, Volume 8, pp. 104-182. New York: Academic Press, 1964.

8. Ffowcs-Williams, J.E. "The Noise from Turbulence Convected at High Speed". *Philosophical Transactions of the Royal Society of London*, Series A, Volume 255, 1963, pp. 469-503.

9. Morse, P.M. and Ingard, K.U. *Theoretical Acoustics*. Princeton University Press, 1986.

10. http://www.apple.com/macosx/

11. Thomas, R.H., Kinzie, K.W., and Pao, S.P. "Computational Analysis of a Pylon-Chevron Core Nozzle Interaction." AIAA-2001-2185, May 2001.

12. Massey, S.J., Thomas, R.H., Abdol-Hamid, K.S., and Elmiligui, A. "Computational and Experimental Flowfield Analyses of Separate Flow Chevron Nozzles and Pylon Interaction". AIAA-2003-3212, May 2003.

13. Pao, S.P., and Abdol-Hamid, K.S. "Numerical Simulation of Jet Aerodynamics Using a Three Dimensional Navier Stokes Method (PAB3D)". NASA TP-3596, September 1996.

14. Abdol-Hamid, K.S., Pao, S.P., Massey, S.J., and Elmiligui, A. "Temperature Corrected Turbulence Model for High Temperature Jet Flow". AIAA-2003-4070, June 2003.

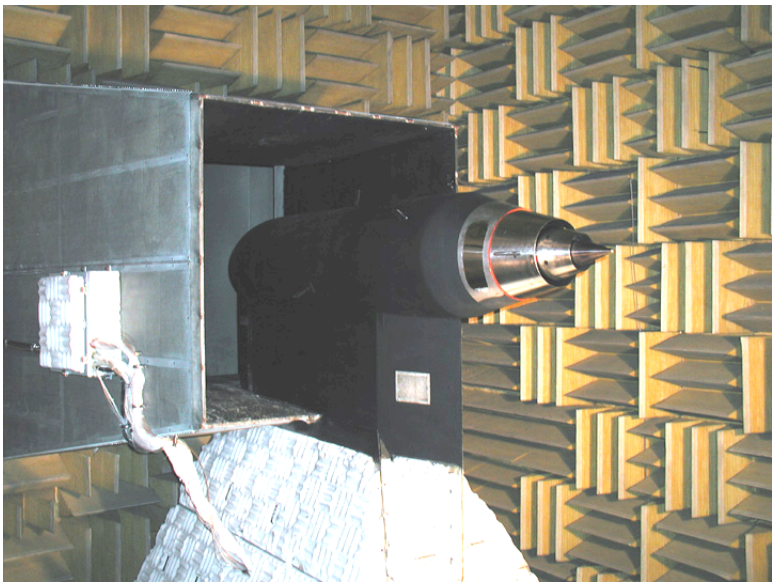

Figure 1: Configuration 1 Nozzle Installed in the NASA Langley JNL-LSAWT for Testing

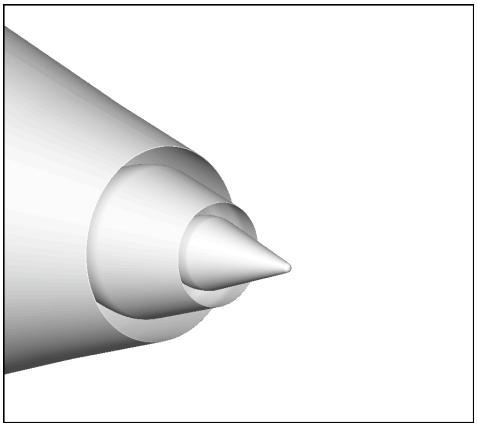

Figure 2: Configuration 1

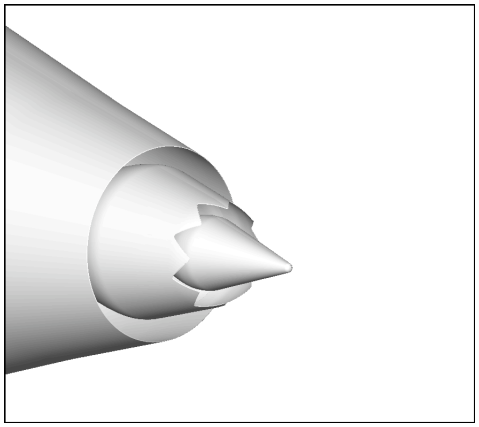

Figure 4: Configuration 3

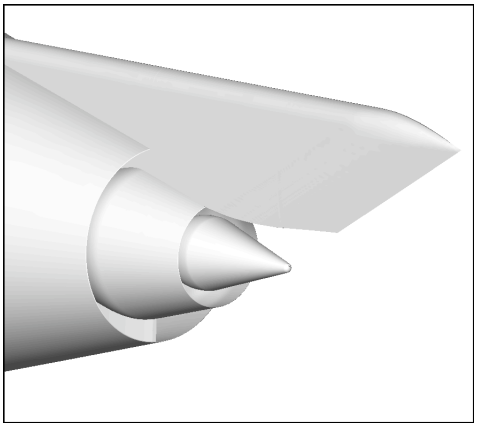

Figure 3: Configuration 6

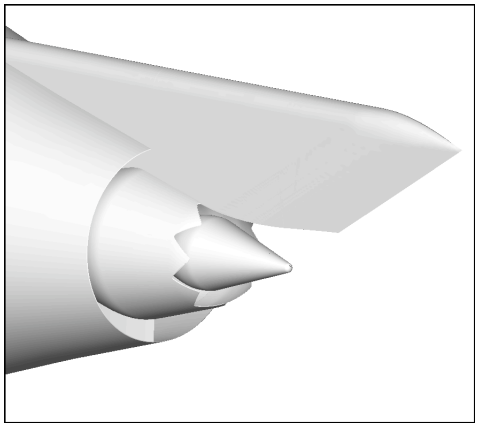

Figure 5: Configuration 4F

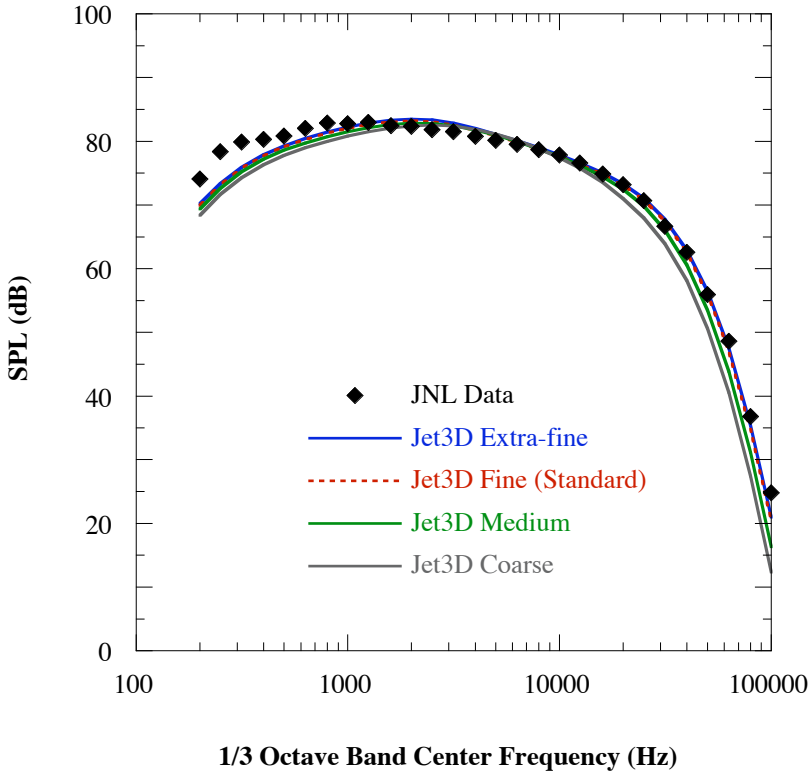

Figure 6: SPL Results from Grid Dependence Study
Configuration 1 – Observer at an Inlet angle of 88°

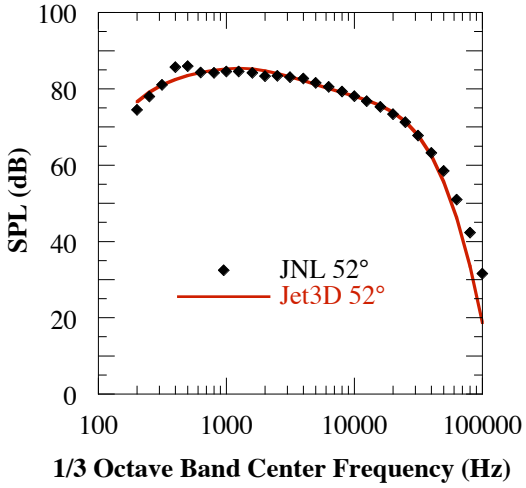

Figure 7A: Configuration 1 SPL at 52° Inlet Angle

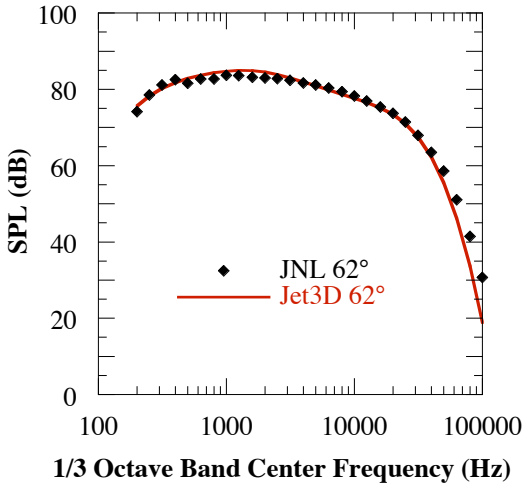

Figure 7B: Configuration 1 SPL at 62° Inlet Angle

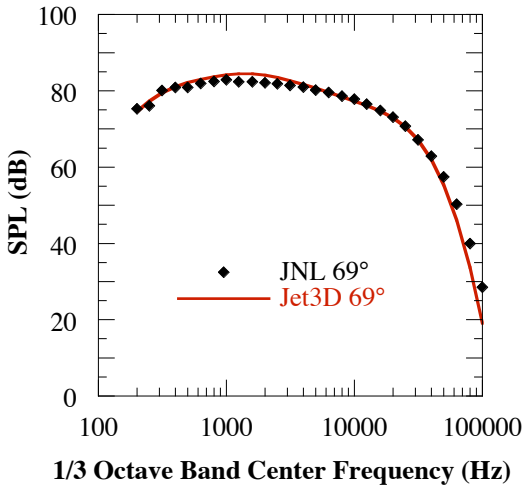

Figure 7C: Configuration 1 SPL at 69° Inlet Angle

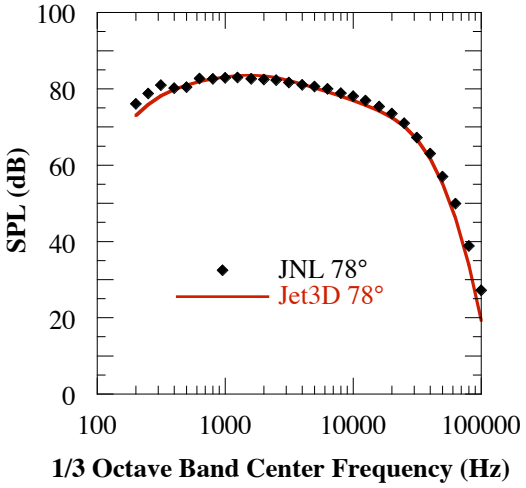

Figure 7D: Configuration 1 SPL at 78° Inlet Angle

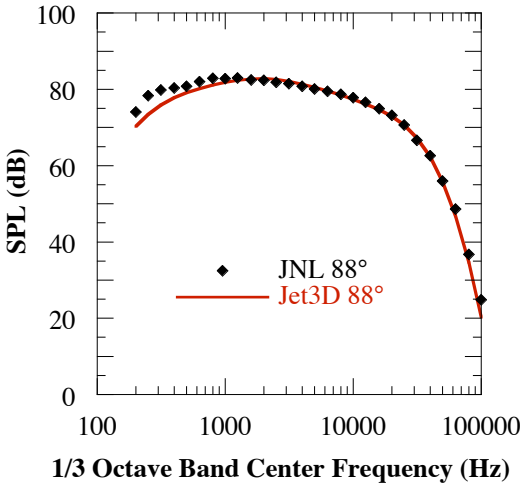

Figure 7E: Configuration 1 SPL at 88° Inlet Angle

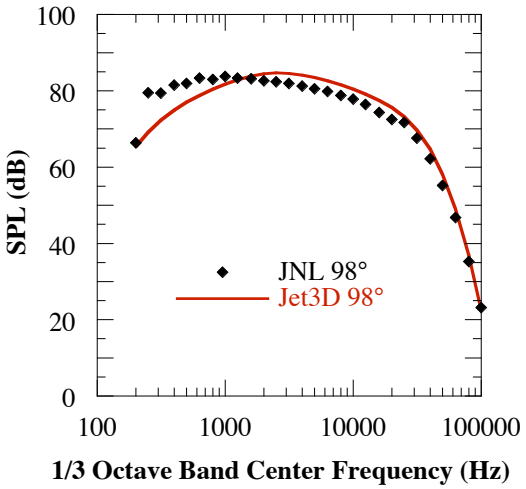

Figure 7F: Configuration 1 SPL at 98° Inlet Angle

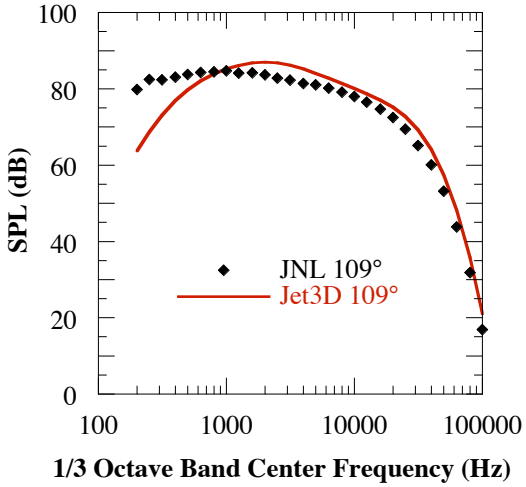

Figure 7G: Configuration 1 SPL at 109° Inlet Angle

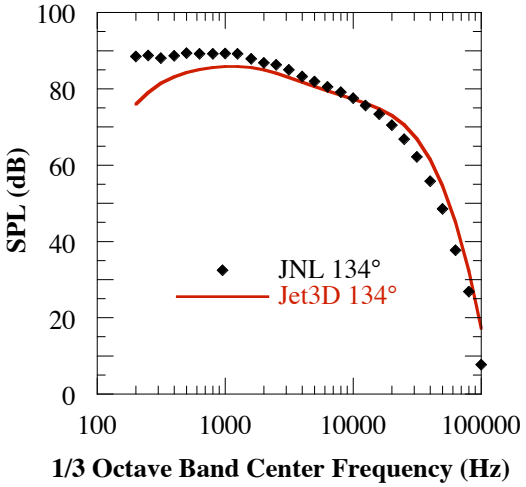

Figure 7J: Configuration 1 SPL at 134° Inlet Angle

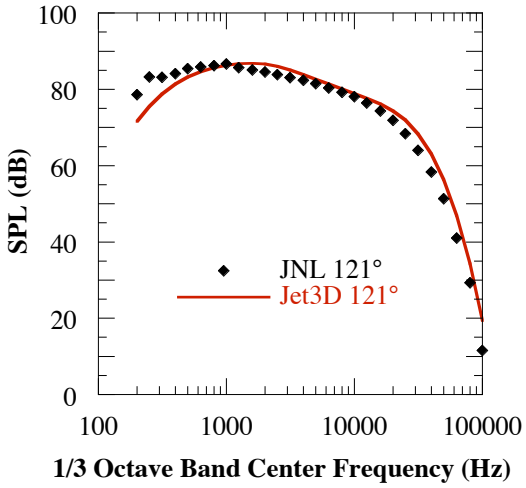

Figure 7H: Configuration 1 SPL at 121° Inlet Angle

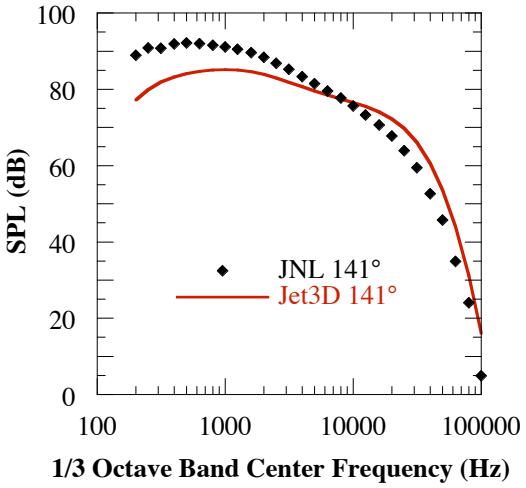

Figure 7K: Configuration 1 SPL at 141° Inlet Angle

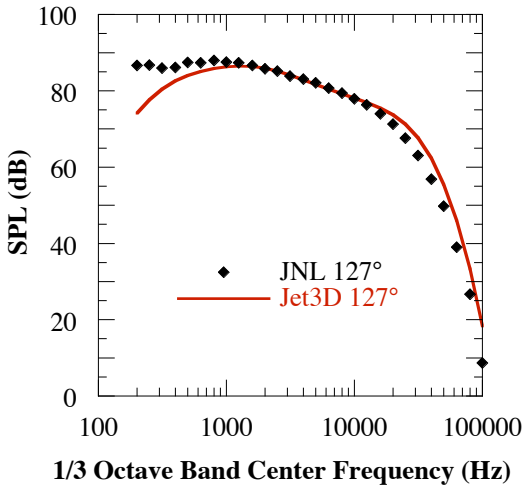

Figure 7I: Configuration 1 SPL at 127° Inlet Angle

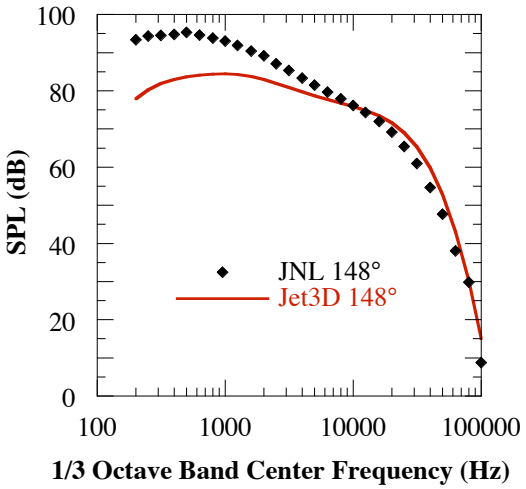

Figure 7L: Configuration 1 SPL at 148° Inlet Angle

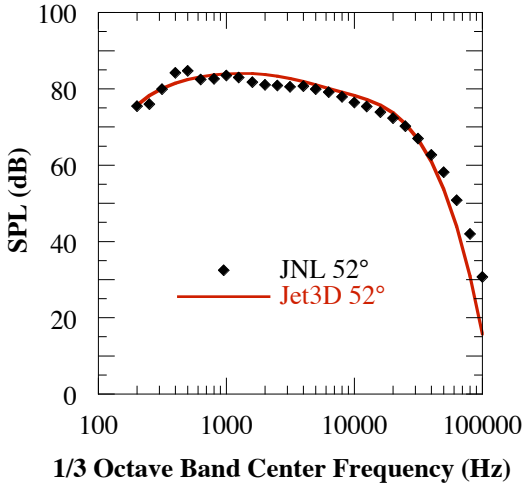

Figure 8A: Configuration 6 SPL at 52° Inlet Angle

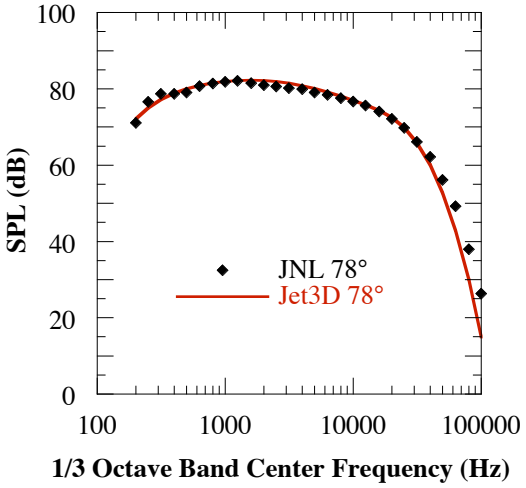

Figure 8D: Configuration 6 SPL at 78° Inlet Angle

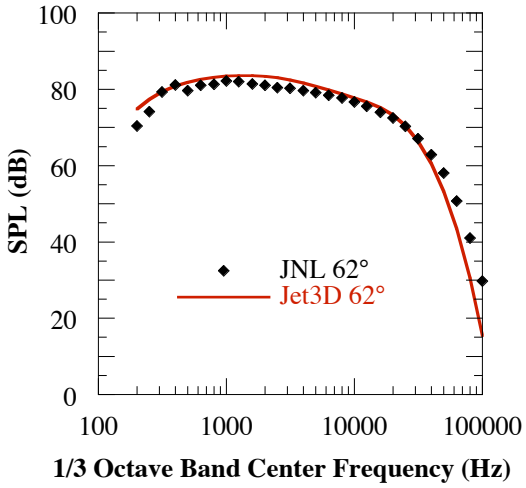

Figure 8B: Configuration 6 SPL at 62° Inlet Angle

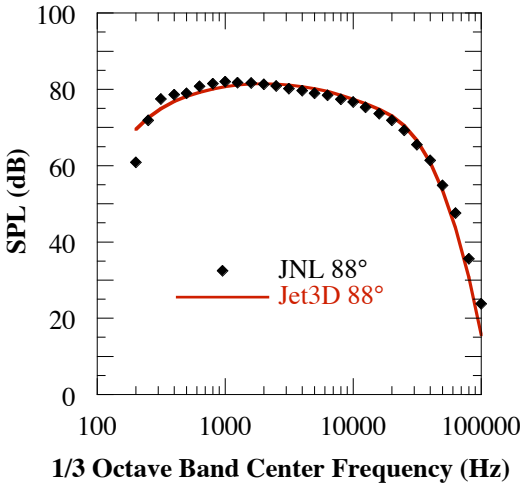

Figure 8E: Configuration 6 SPL at 88° Inlet Angle

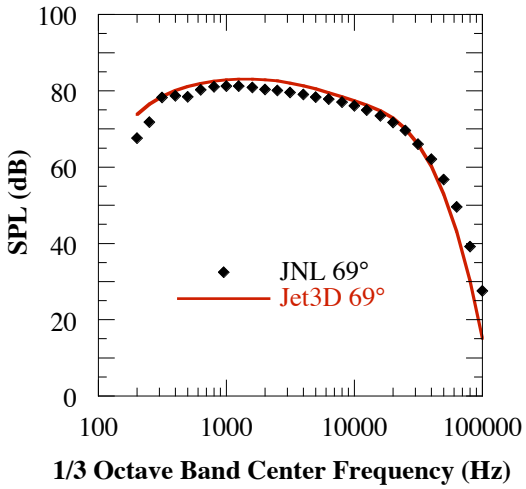

Figure 8C: Configuration 6 SPL at 69° Inlet Angle

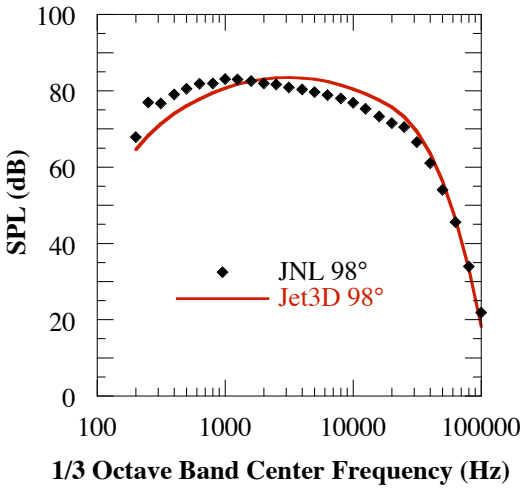

Figure 8F: Configuration 6 SPL at 98° Inlet Angle

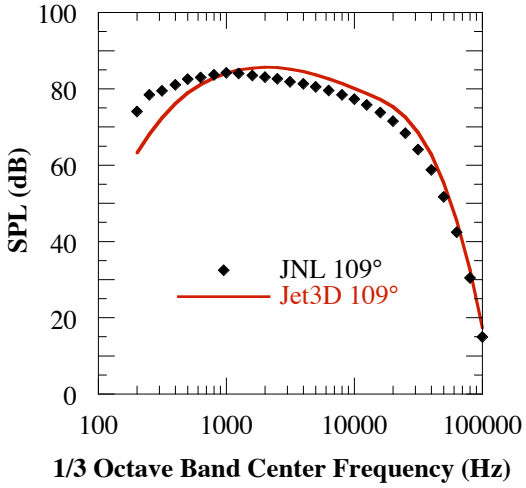

Figure 8G: Configuration 6 SPL at 109° Inlet Angle

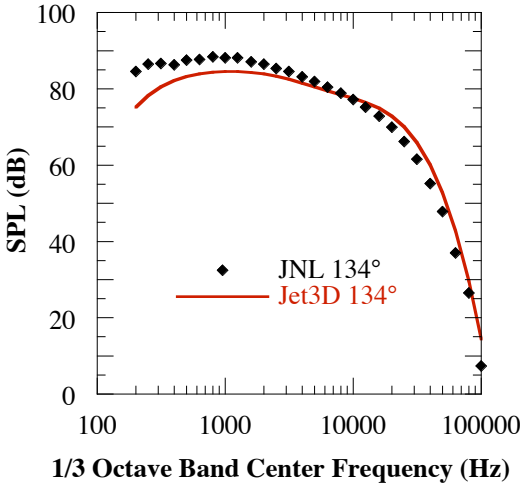

Figure 8J: Configuration 6 SPL at 134° Inlet Angle

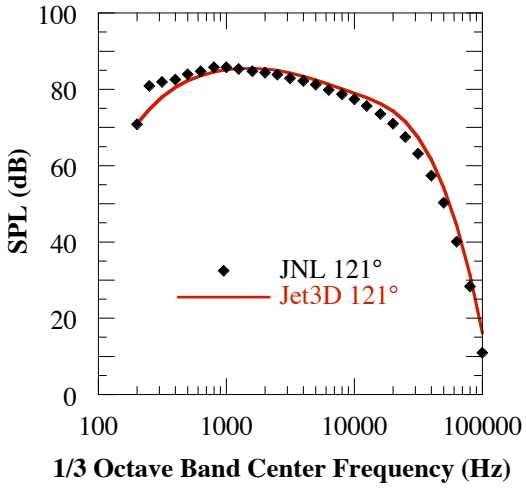

Figure 8H: Configuration 6 SPL at 121° Inlet Angle

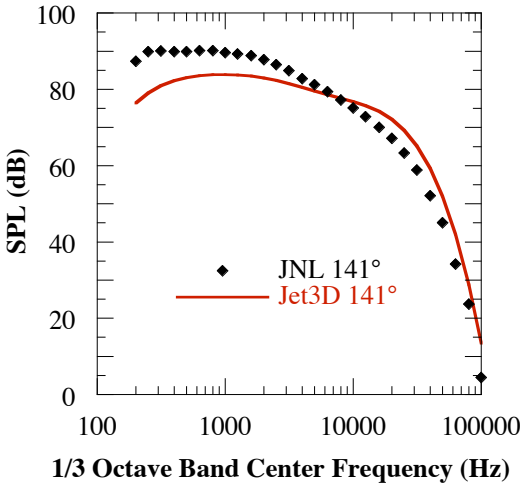

Figure 8K: Configuration 6 SPL at 141° Inlet Angle

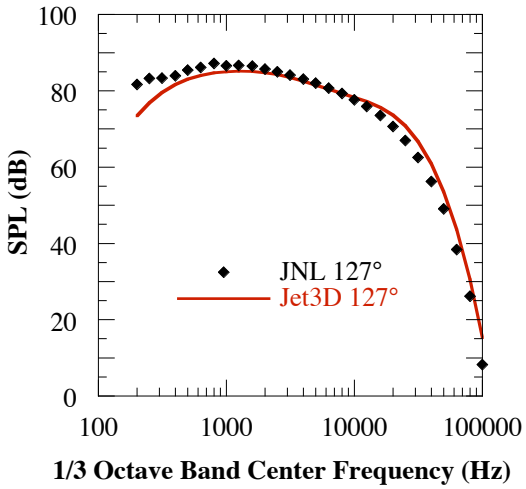

Figure 8I: Configuration 6 SPL at 127° Inlet Angle

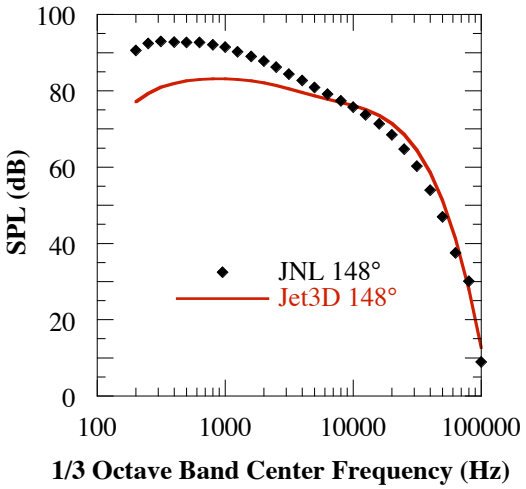

Figure 8L: Configuration 6 SPL at 148° Inlet Angle

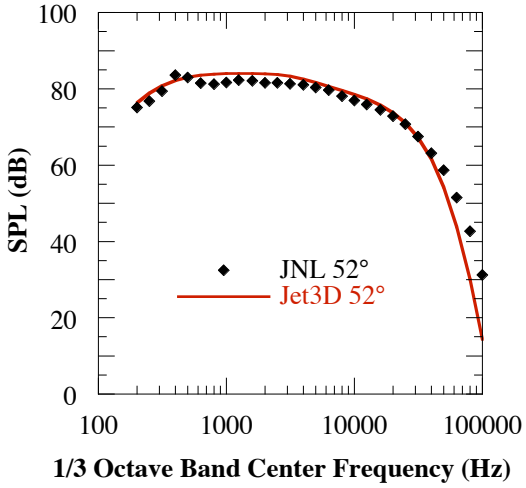

Figure 9A: Configuration 3 SPL at 52° Inlet Angle

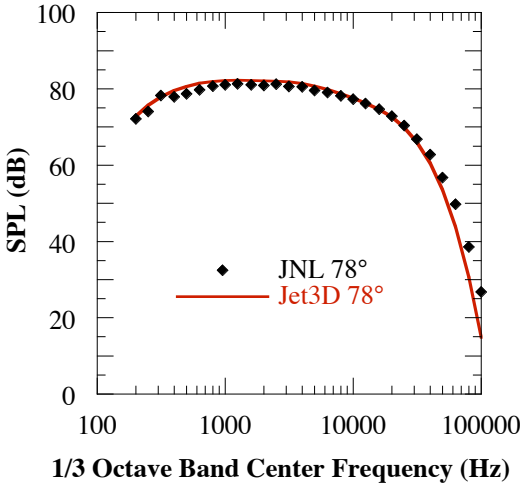

Figure 9D: Configuration 3 SPL at 78° Inlet Angle

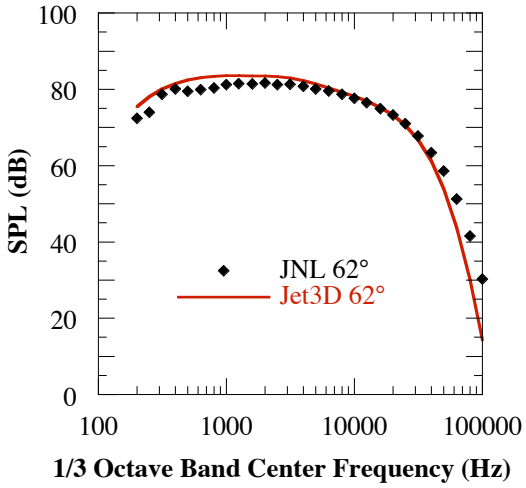

Figure 9B: Configuration 3 SPL at 62° Inlet Angle

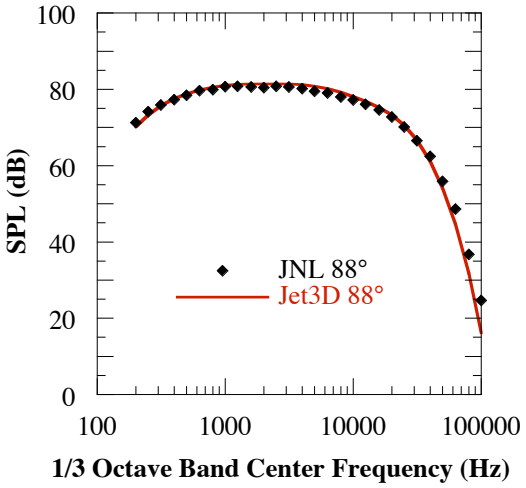

Figure 9E: Configuration 3 SPL at 88° Inlet Angle

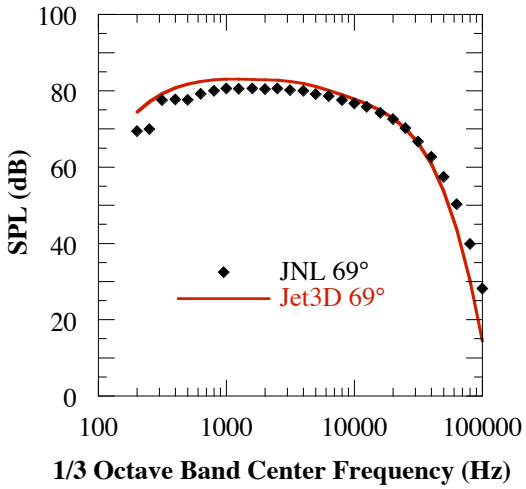

Figure 9C: Configuration 3 SPL at 69° Inlet Angle

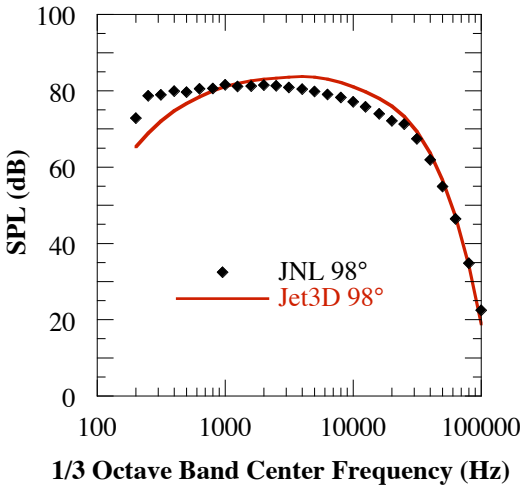

Figure 9F: Configuration 3 SPL at 98° Inlet Angle

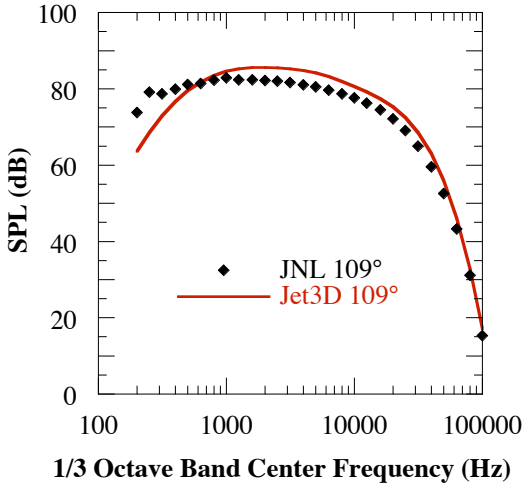

Figure 9G: Configuration 3 SPL at 109° Inlet Angle

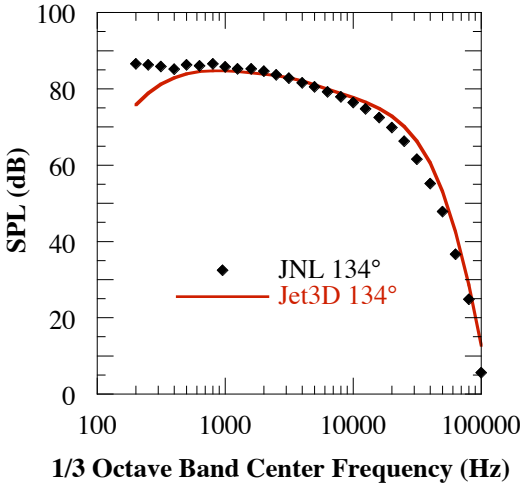

Figure 9J: Configuration 3 SPL at 134° Inlet Angle

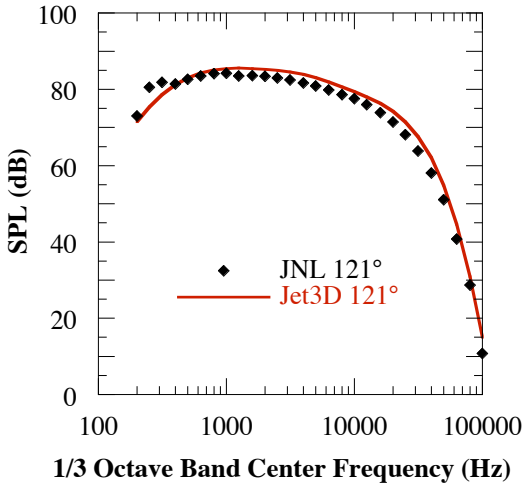

Figure 9H: Configuration 3 SPL at 121° Inlet Angle

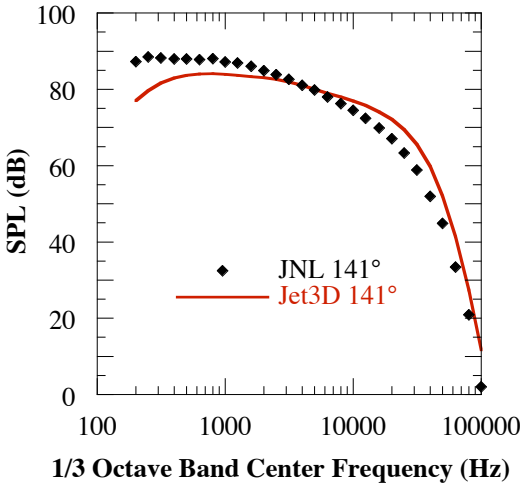

Figure 9K: Configuration 3 SPL at 141° Inlet Angle

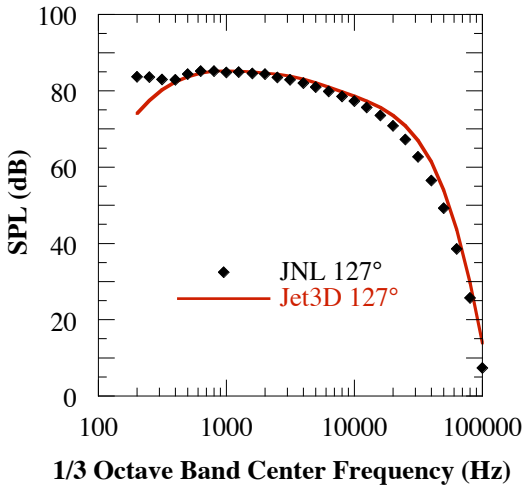

Figure 9I: Configuration 3 SPL at 127° Inlet Angle

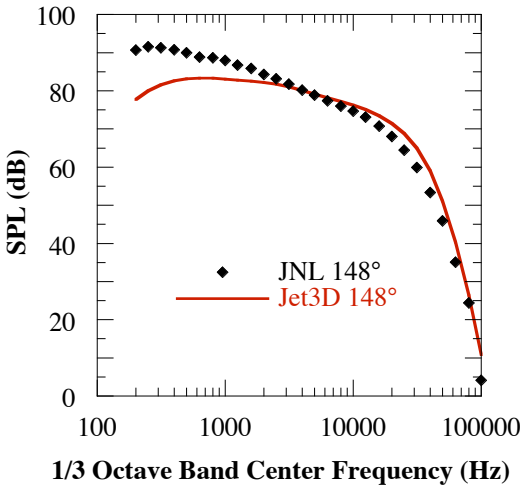

Figure 9L: Configuration 3 SPL at 148° Inlet Angle

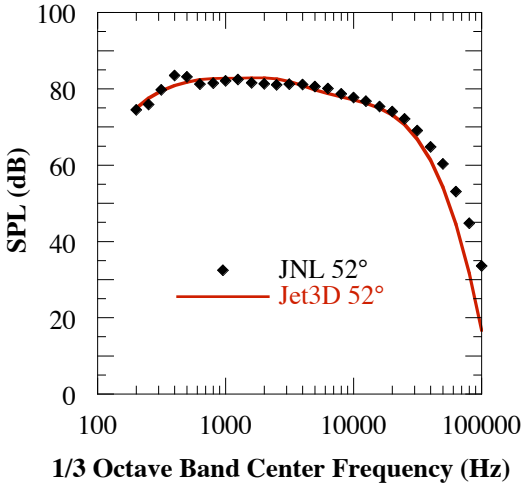

Figure 10A: Configuration 4F SPL at 52° Inlet Angle

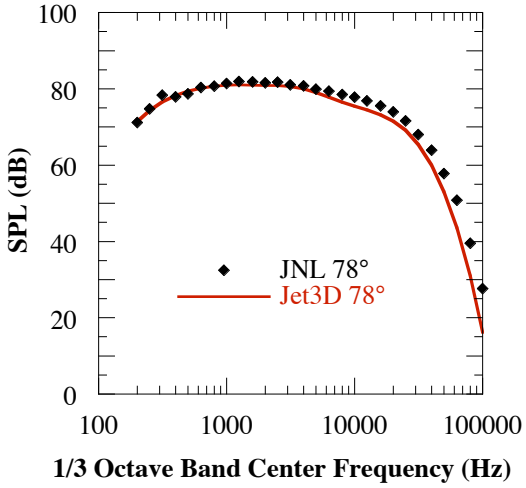

Figure 10D: Configuration 4F SPL at 78° Inlet Angle

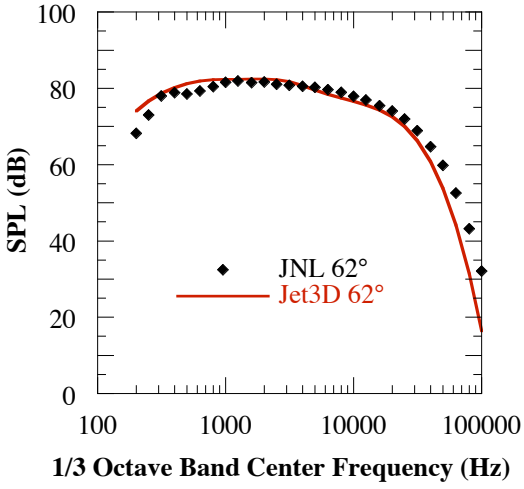

Figure 10B: Configuration 4F SPL at 62° Inlet Angle

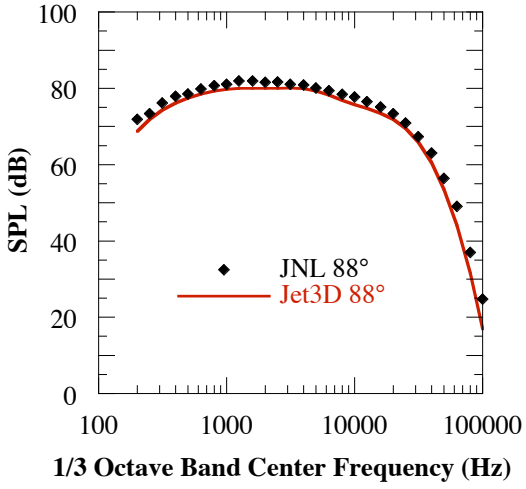

Figure 10E: Configuration 4F SPL at 88° Inlet Angle

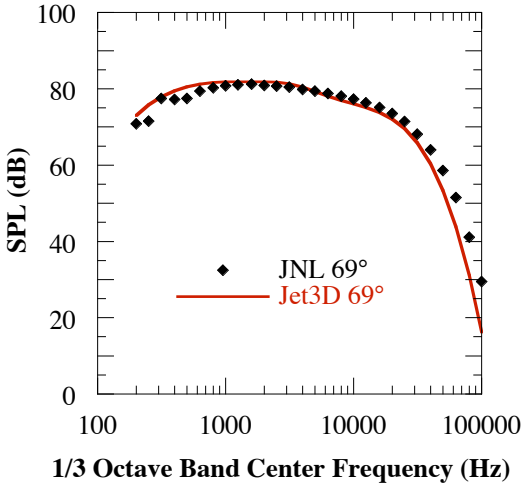

Figure 10C: Configuration 4F SPL at 69° Inlet Angle

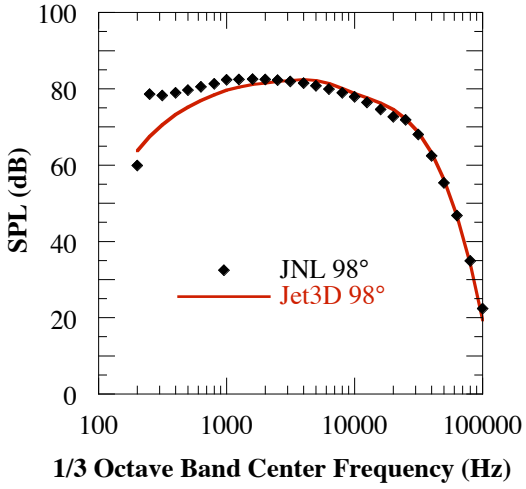

Figure 10F: Configuration 4F SPL at 98° Inlet Angle

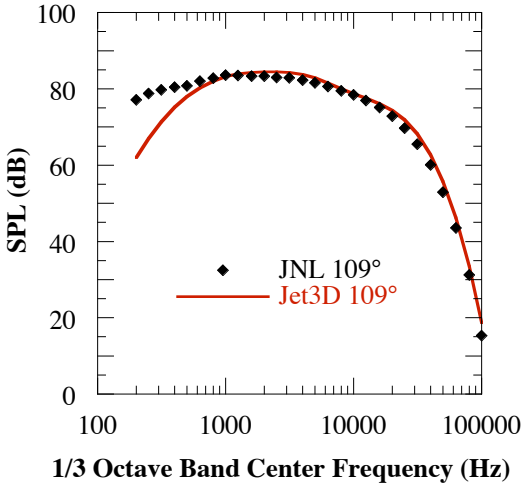

Figure 10G: Configuration 4F SPL at 109° Inlet Angle

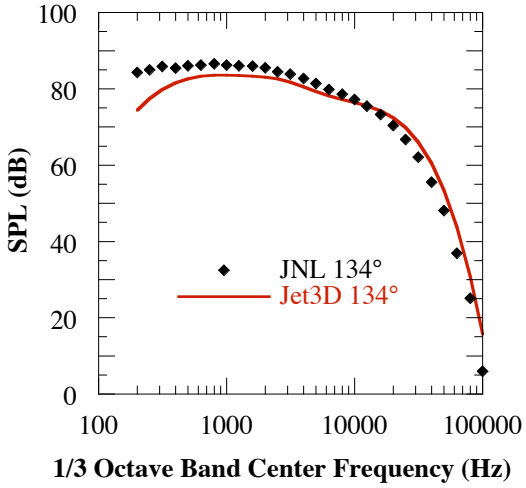

Figure 10J: Configuration 4F SPL at 134° Inlet Angle

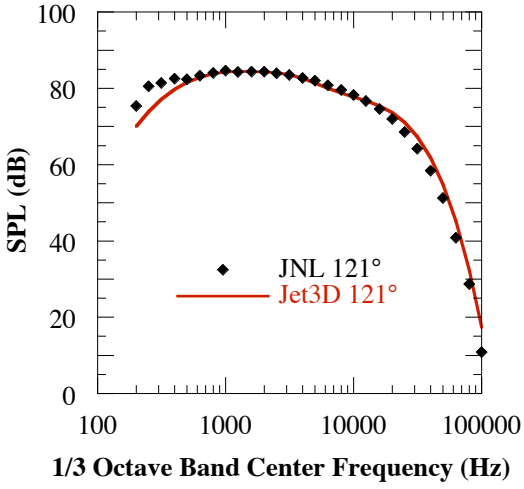

Figure 10H: Configuration 4F SPL at 121° Inlet Angle

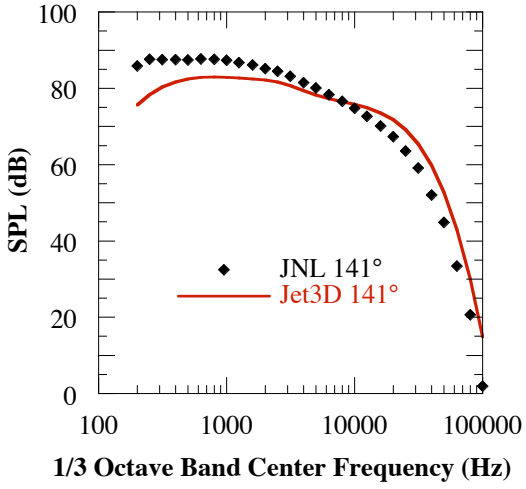

Figure 10K: Configuration 4F SPL at 141° Inlet Angle

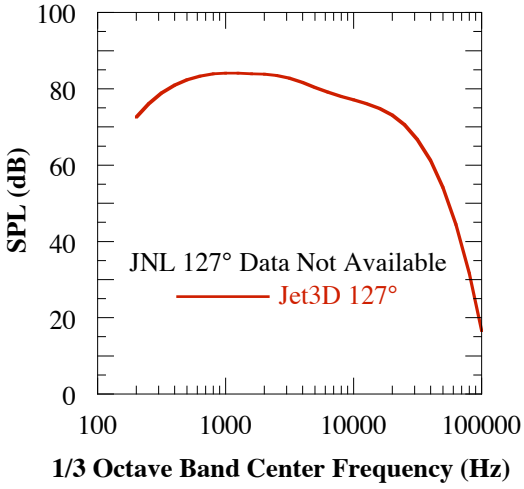

Figure 10I: Configuration 4F SPL at 127° Inlet Angle

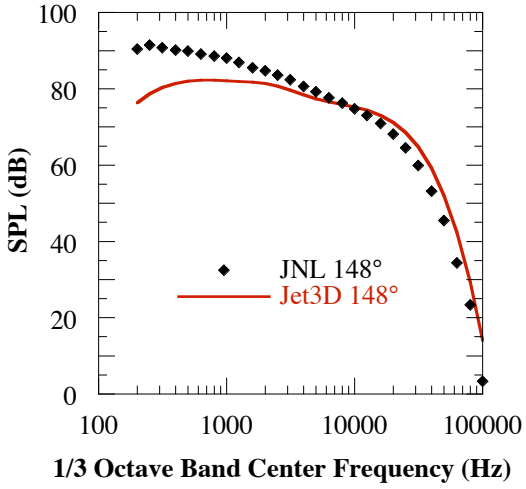

Figure 10L: Configuration 4F SPL at 148° Inlet Angle

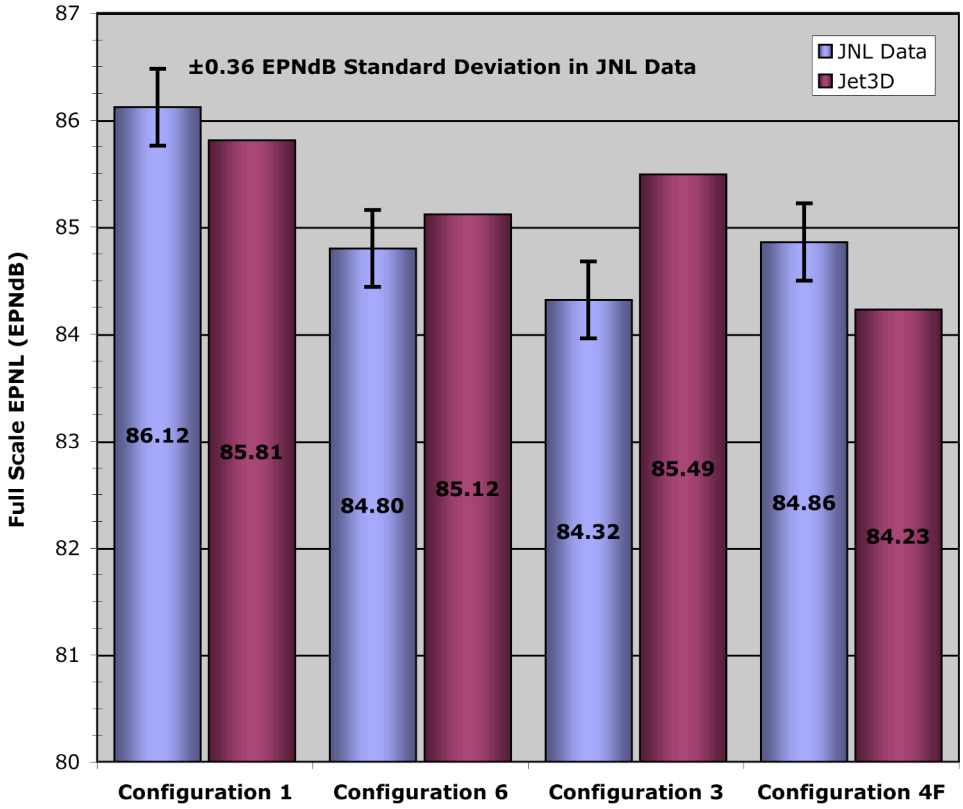

Figure 11: Comparison of Full-Scale EPNL

EPNLs for a full-scale (scale factor 9.0) M=0.28 flyover, at a distance of 543m (1782ft), typical of certification. This corresponds to an altitude of 305m (1000ft) and a ground sideline distance of 450m (1476ft).

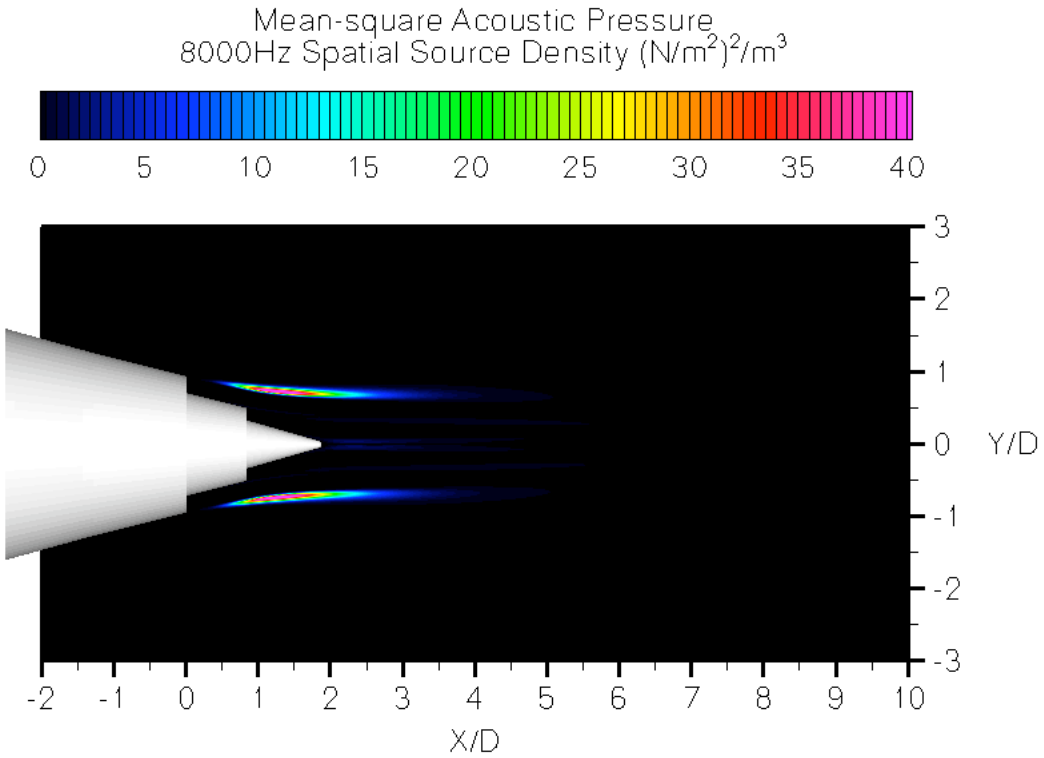

Figure 12: Noise Map at 8000 Hz, Observer at 121° Inlet Angle - Configuration 1
**(Observer Location: X/D=59.7, Y/D=0.0, Z/D=-26.1)*

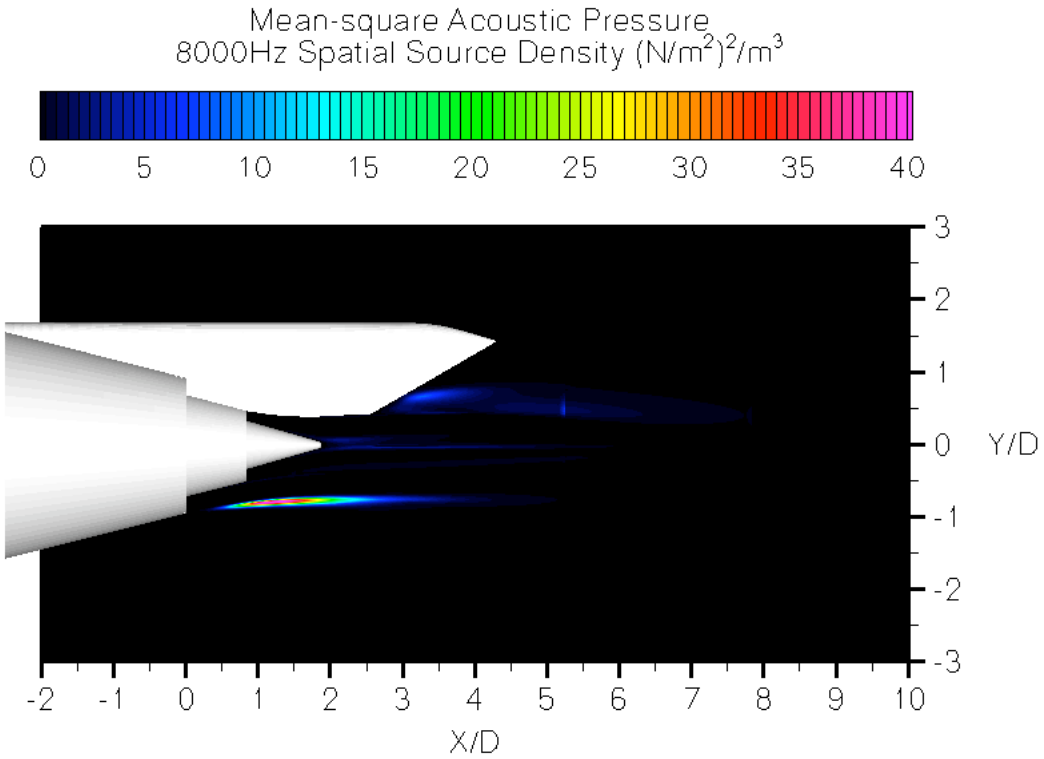

Figure 13: Noise Map at 8000 Hz, Observer at 121° Inlet Angle - Configuration 6
**(Observer Location: X/D=59.7, Y/D=0.0, Z/D=-26.1)*

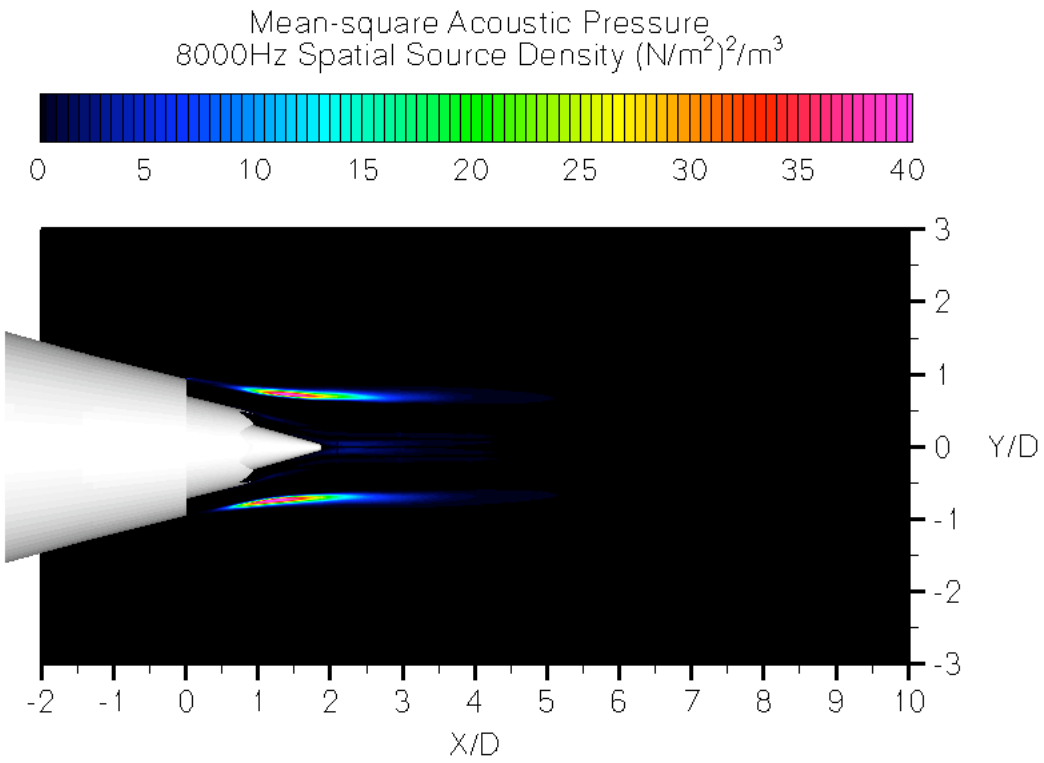

Figure 14: Noise Map at 8000 Hz, Observer at 121° Inlet Angle - Configuration 3
**(Observer Location: X/D=59.7, Y/D=0.0, Z/D=-26.1)*

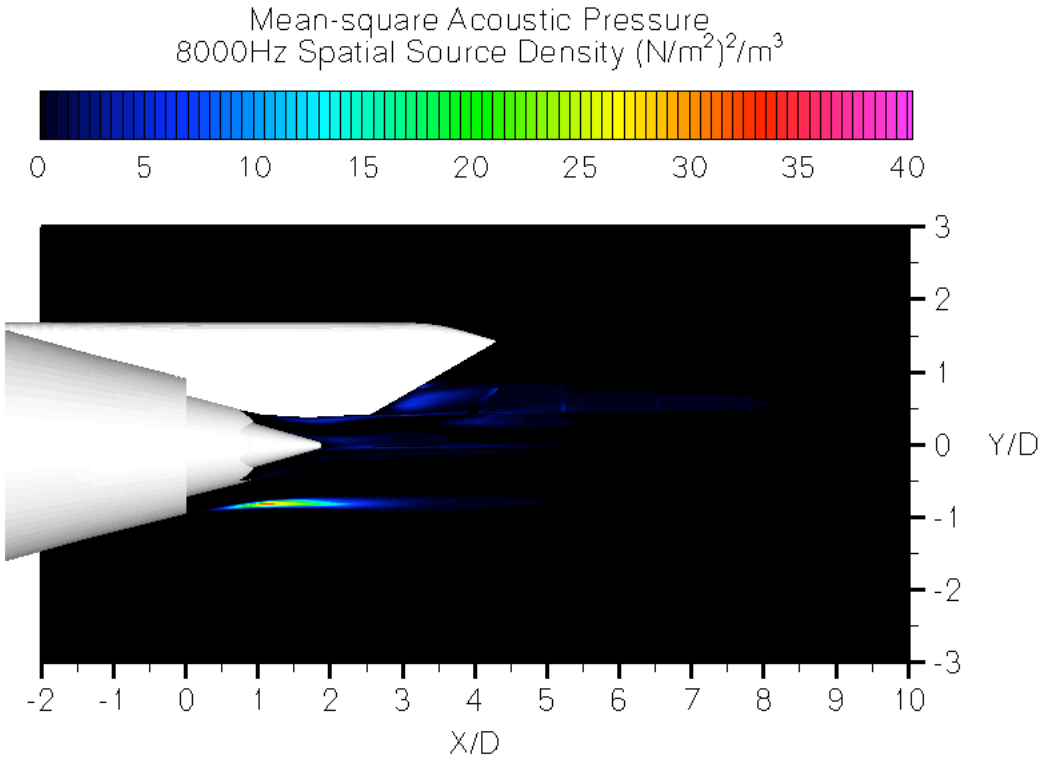

Figure 15: Noise Map at 8000 Hz, Observer at 121° Inlet Angle - Configuration 4F
**(Observer Location: X/D=59.7, Y/D=0.0, Z/D=-26.1)*

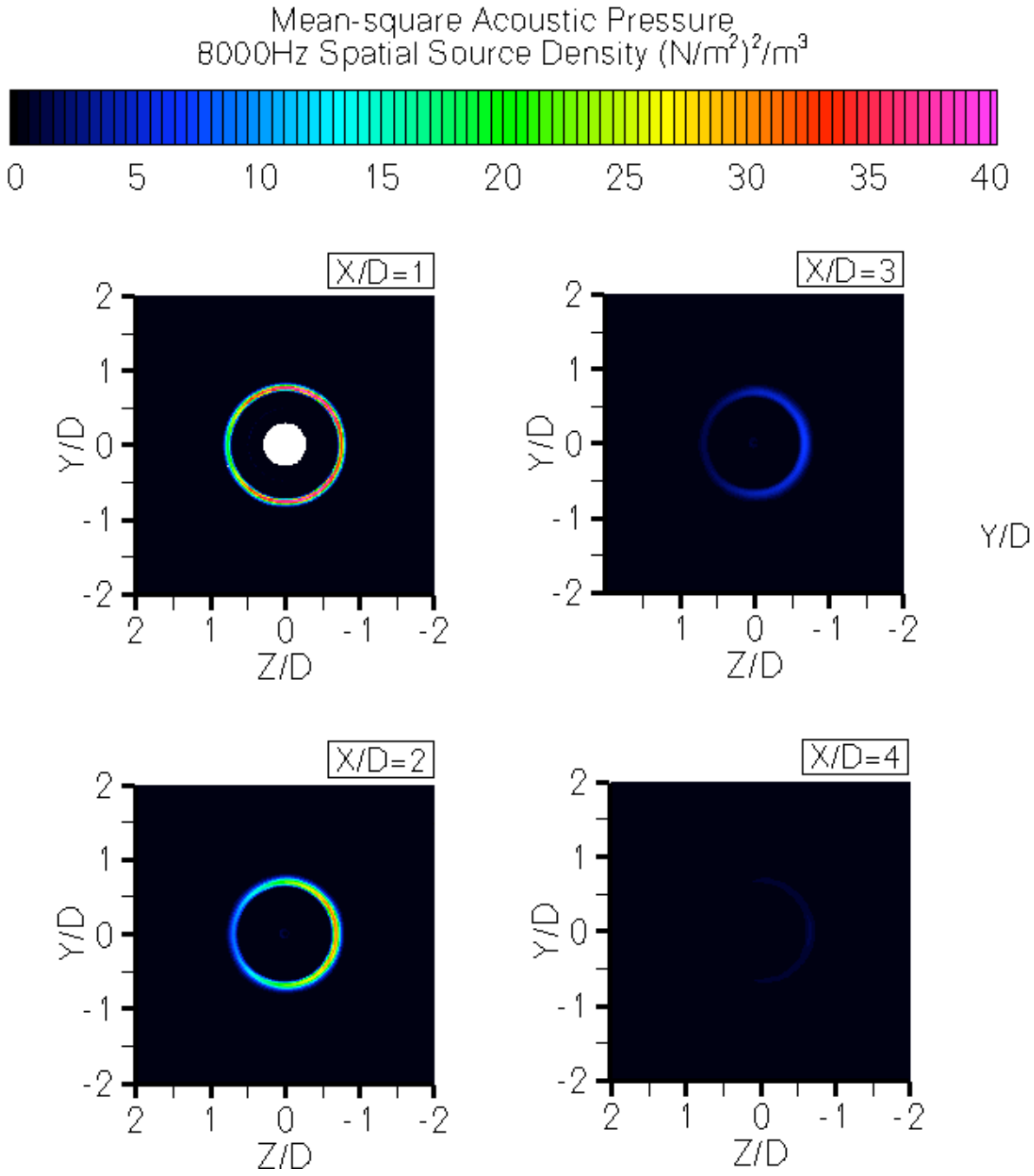

Figure 16: Crossflow Noise Maps at 8000 Hz, Observer at 121° Inlet Angle - Configuration 1.*
**(Observer Location: X/D=59.7, Y/D=0.0, Z/D=-26.1)*

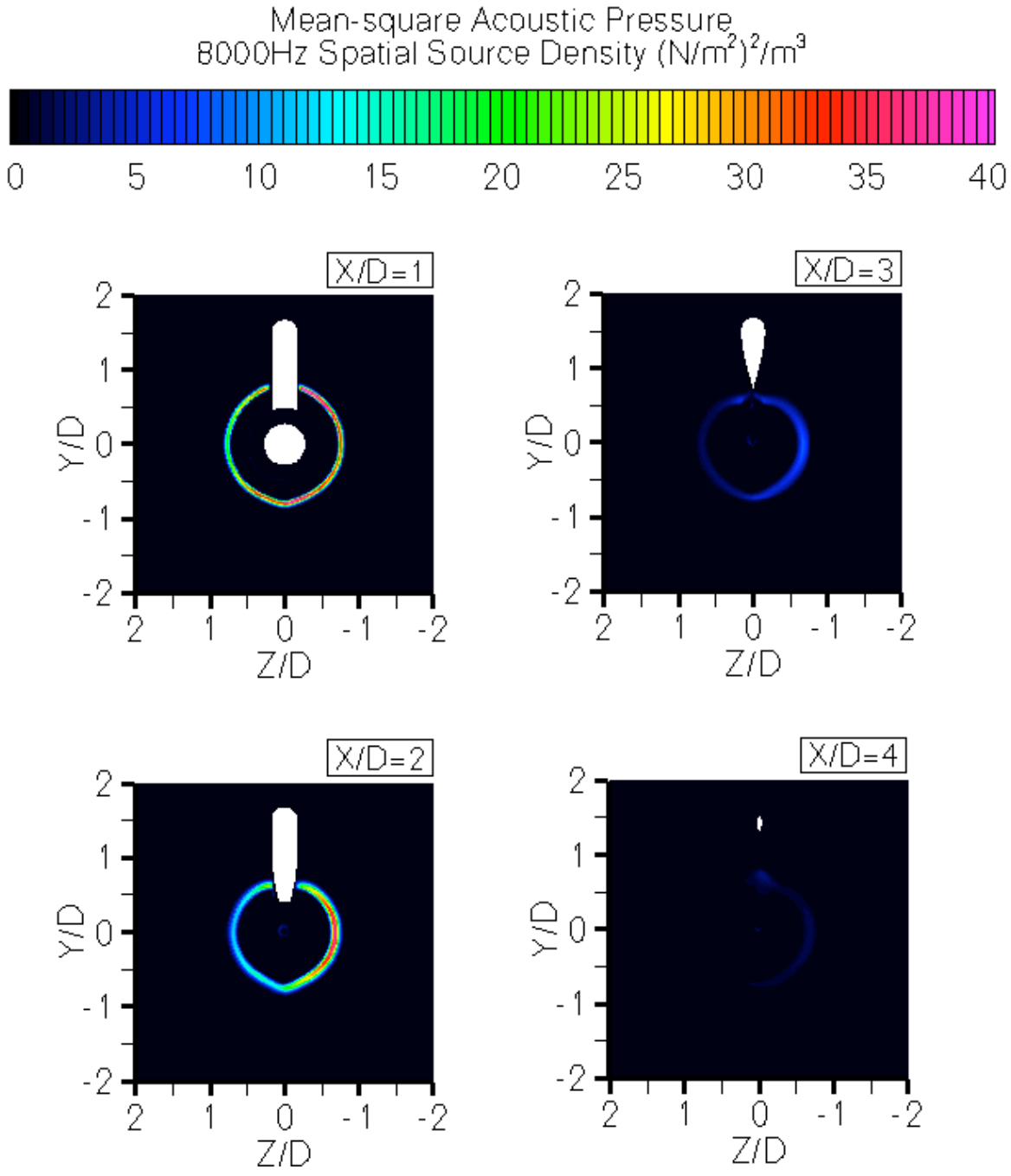

Figure 17: Crossflow Noise Maps at 8000 Hz, Observer at 121° Inlet Angle - Configuration 6.*
**(Observer Location: X/D=59.7, Y/D=0.0, Z/D=-26.1)*

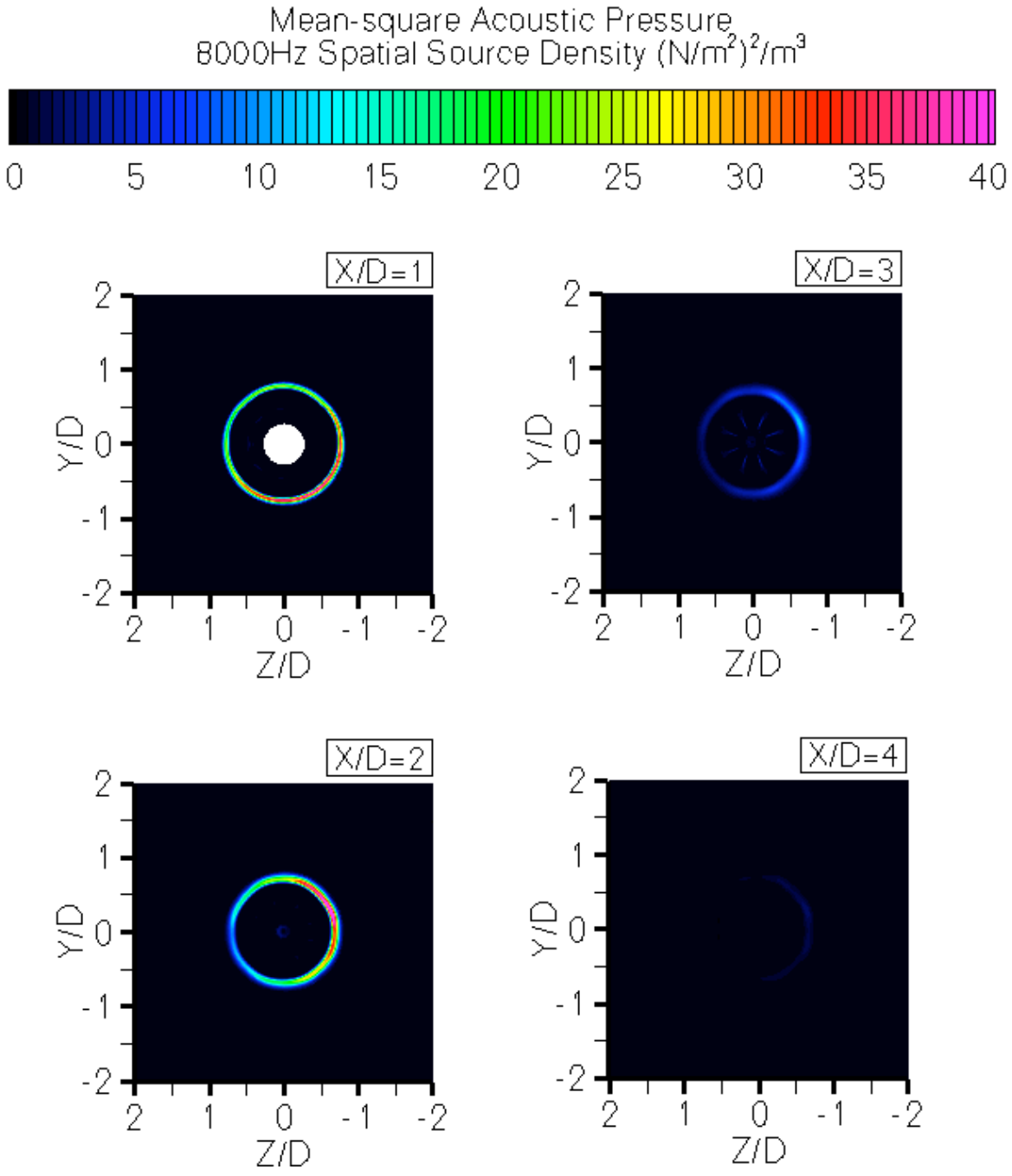

Figure 18: Crossflow Noise Maps at 8000 Hz, Observer at 121° Inlet Angle - Configuration 3.*
**(Observer Location: X/D=59.7, Y/D=0.0, Z/D=-26.1)*

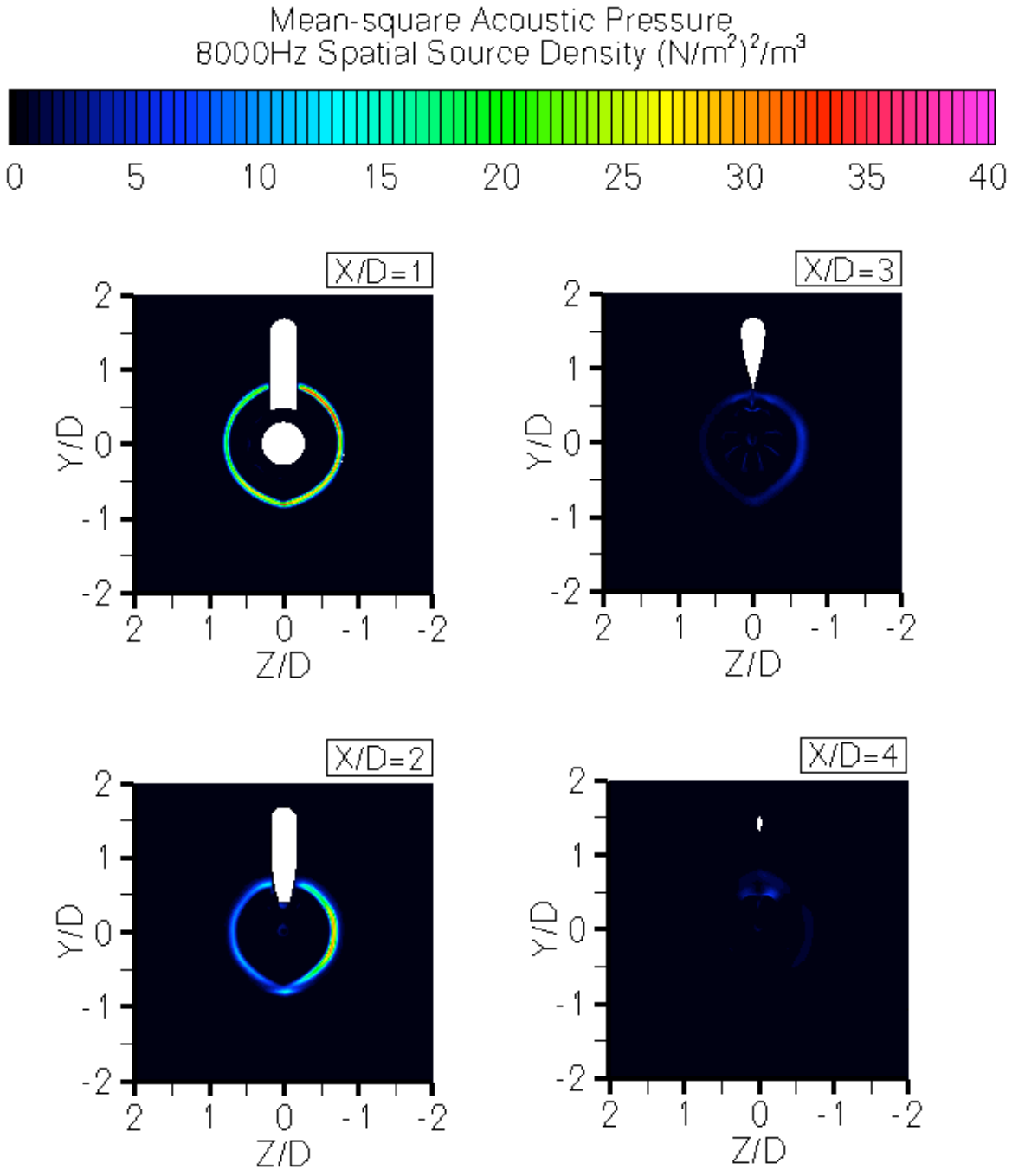

Figure 19: Crossflow Noise Maps at 8000 Hz, Observer at 121° Inlet Angle - Configuration 4F.*
**(Observer Location: X/D=59.7, Y/D=0.0, Z/D=-26.1)*